2012•2013
FACULTEIT GENEESKUNDE EN LEVENSWETENSCHAPPEN
master in de biomedische wetenschappen: bio-elektronica en nanotechnologie

Masterproef
Synthesis and characterization of arrays of metal oxide nanowires with highly controllable diameters for future sensor applications

Promotor :
Prof. dr. Hans-Gerhard BOYEN

De transnationale Universiteit Limburg is een uniek samenwerkingsverband van twee universiteiten in twee landen: de Universiteit Hasselt en Maastricht University.

Kaï Betlem
Masterproef voorgedragen tot het bekomen van de graad van master in de biomedische wetenschappen , afstudeerrichting bio-elektronica en nanotechnologie

universiteit hasselt
►►**KNOWLEDGE IN ACTION**

universiteit hasselt | **Maastricht University**

Masterproef

Synthesis and characterization of arrays of metal
oxide nanowires with highly controllable diameters for
future sensor applications

Promotor :
Prof. dr. Hans-Gerhard BOYEN

Kaï Betlem
*Masterproef voorgedragen tot het bekomen van de graad van master in de biomedische
wetenschappen , afstudeerrichting bio-elektronica en nanotechnologie*

universiteit
►►hasselt | Maastricht University

Abstract

Tin oxide (SnO_2) is a semiconducting material with a high transparency, a low resistivity and a high biocompatibility. With these properties SnO_2-based sensors could be used in many fields, ranging from the detection of gasses to the detection of light. To increase the sensitivity of such a sensor the surface-to-volume ratio has to be increased. This can be achieved by patterning on the nanometer scale or, in other words, by synthesizing 1D nanostructures in a very high density at the surface of an appropriate substrate. When the nanowires become small enough in diameter (<10 nm) quantum size effects start to play an increasingly important role thus influencing all properties of the nanowires. When creating nanowires with the Vapour Liquid Solid (VLS) method the diameter of the wires usually depends on the diameter of the catalyst particle used to synthesize the wires. However, diameters below 20nm are difficult to achieve via VLS even with catalyst sizes well below 10 nm. Creating very thin nanowires (diameter <10 nm) in a controlled way thus has been and still remains a highly challenging task.

This study will make use of the micellar approach to deposit ultra-high density arrays of gold particles being used as catalysts with sizes well below 10 nm and a narrow size distribution for the subsequent growth of SnO_2 nanowires via chemical vapour deposition in a tube furnace system. The main objective of this work is to identify and optimize all relevant growth parameters that allow to finally synthesize such nanowires with diameters approaching or even passing the threshold for inducing quantum size effects (< 10nm) in a highly controlled way.

Table of Contents

Acknowledgements

Abbreviations

AFM	Atomic Force Microscopy
CVD	Chemical Vapour Deposition
FE-SEM	field emission scanning electron microscopy
PS	polystyrene
P2VP	block-poly(2-vinylpyridine)
US	ultrasound
VS	vapour–solid
VSS	Vapour-solid-solid
VLS	vapour-liquid-solid
XPS	X-ray photoelectron spectroscopy

Introduction

Nanotechnology is nowadays a well know concept related to objects with reduced dimensions. The concept was first introduced in 1959 by Richard Feynman in his talk "*There's Plenty of Room at the Bottom*",[1] but it took some time to come to live. The term nano was also introduced during that time to the SI-system as a prefix for the 10^{-9} size factor.[2] A nanostructure is an object that has at least one dimension below 100 nm.[3] Depending on how many of the spatial dimensions are limited this creates so-called 0D (quantum dots), 1D (nanowires, nanotubes, nanorods and nanobelts), or 2D (quantum well) nanostructures. The 1D structures receive a lot of attention lately from many different fields, for example photon emission and absorption,[4] metal-to-insulator transition in a material,[5] semiconduction,[6] electrochemical and electro mechanics,[3] magnetism,[7] and biotechnology.[8] These 1D structures have their own specific properties compared to the other dimensional structures, but for all of them the properties depend on the shape, size and composition of the nanoscaled object. Nanowires which are in the focus of this work are one of the possible shapes of the 1D structures besides other possible shapes like nanofibres, whiskers, nanorods, nanobelts, nanoribbons and nanotubes [9] presented in Figure 1.
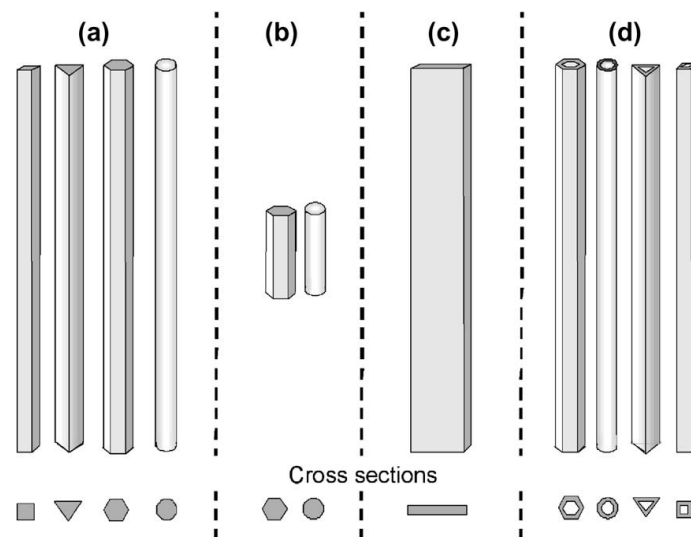
Figure 1 shows the different 1D nanostructures that can be created: (a) nanowires, nanofibres or whiskers; (b) nanorods; (c) nanobelts or nanoribbons and (d) nanotubes.

Nanowires can be made from different materials like metals, carbon or even rare-earth compounds (hydroxides, oxides, oxysulfides, oxyhalides).[10] The material the wires are made of determines to a large extent their properties such as catalytic, electronic, optical magnetic, and biological behaviour.[10] Tin oxide (SnO_2) is a wide band gap semiconductor which is chemically inert and which has a high transparency and low resistivity.[11, 12] Because of these properties it is currently commercially used in environmental monitoring, industrial electronic sensing, liquid crystal displays, etc.[13] The SnO_2 nanowires are further actively investigated in the fields of photoluminescence,[14] lashing,[15] field emission,[16] transistors, solar cells,[17] and for battery applications.[18, 19] Finally, and perhaps of most importance, SnO_2 is found to be biocompatible.[20-23] This makes it a very attractive material to be used in bio-electronics and biosensing. Not just to detect biological compounds, but also to look inside

living cells,[24] or to be used as a therapeutics or antiviral agent that has the ability to suppress diseases such as Herpes Simplex virus 1 and 2 (HVS-1 and HVS-2).[25]

The use of SnO_2 in chemo-sensor applications is already known where it is able to detect gasses such as CO, NO, NO_2, NO_3, NH_3, N, O, O_3, H_2O LPG, ethanol and a large range of other carbonic compounds including certain nerve toxins. In addition, it can also be used to detect light.[25-29] The readout of the sensor can be realized by impedance or voltage/current measurements for which mostly elevated temperatures are needed.[25, 29]

The diameter of a nanowire influences the physical properties, and in some cases, a small change can make a large difference. For example, when working with single wall carbon nanotubes where the n and m values are identical (index of chirality) a small change in diameter will trigger a change in chirality of the wire which itself will determine if the wire will be conductive or semiconductive.[30] When using metallic nanowires, the diameter influences properties like strength,[31] the elastic modulus,[32, 33] magnetic[34] and thermodynamic behaviour.[35] The diameter seems to allow an easy control in order to influence and modify the properties of the nanowires. However, this is still a rather challenging task especially when creating nanowires with diameters around 10 nm and below. Wires of this size are reaching the Fermi wavelength leading to confinement of the electron wave functions (particle in a box problem).[36] The quantum size effects that come into play change the electronic density of states and affect the transport and optical properties of the wires.[37] Besides the quantum size effects, the surface to volume ratio increases with an decrease of the nanowire diameter which can improve the detection limit when such wires are used as sensors.[26]

In order to control the diameter of nanowires there are two general routes, the top-down method and the bottom-up approach.[38] The top-down method makes use of optical lithography which is widely exploited in computer technology to fabricate processors that have double the amount of transistors roughly every 18 months, as predicted by Morse law.[36] The underlying principle is illustrated in Figure 2: here, a mask is imprinted into a photoresist that either hardens or weakens upon illumination depending on the type of resist used. This allows to selectively remove the unwanted parts of the photoresist and to cover the resulting pattern with a metal to create the desired contacts. This technique is able to create transistors with a theoretical limit around 5 nm,[39, 40] however, 22 nm is the current commercial limit.[41]
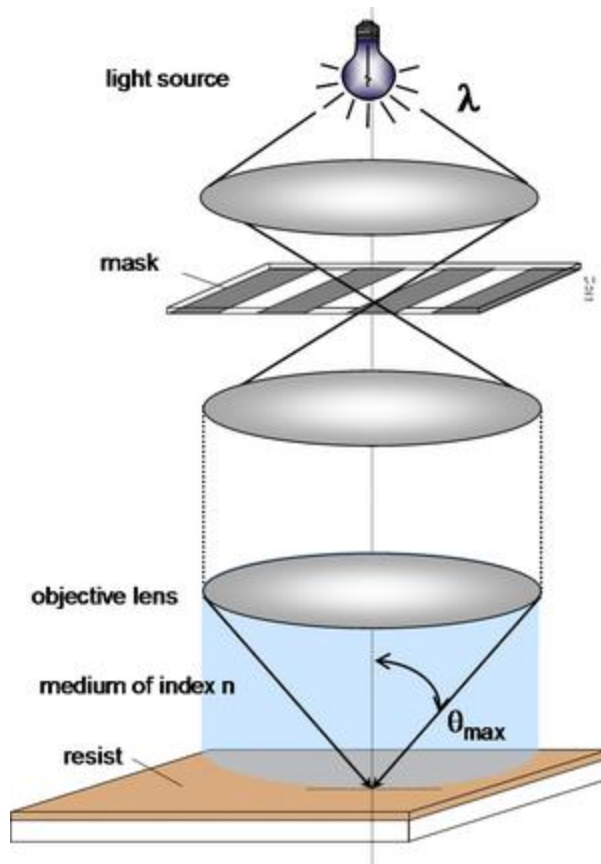
Figure 2: a schematic representation of optical lithography as top-down approach to create nanowires (e.g. interconnects in processors)

The second approach to create rather small items is the bottom-up approach. Here, a nanosized object will self-assemble from its individual building blocks like in case of MIPS[42] or micelles.[43, 44] Micellar structures can be used to create 0D quantum dots out of different metal salts like gold,[45, 46] iron,[47] cobalt,[47] nickel,[47] zinc,[48] silver[46] and others. Such metal particles can subsequently be exploited as catalysts to synthesize 1D nanowires by means of chemical vapour deposition (CVD). Therefore, micellar nanoparticles should have a narrow size distribution at diameters below 10 nm.[44] Such an approach would furthermore allow to spatially organize the catalyst particles into regular patterns, which would be an improvement over more conventional methods to produce catalyst particles like sputtering or evaporation the latter resulting in disordered ensembles which additionally suffer from broad size distributions.[27]

For the synthesis of 1D nanostructures, there are different reaction mechanisms available and it depends on the material that these structures will be made of which mechanism needs be used. On one hand, metal or metal oxide nanowires are often grown by the vapour–solid-solid (VSS) or vapour-liquid-solid (VLS) methods which both rely on the presence of catalyst particles at a substrate surface to grow the nanostructures. On the other hand, nanowires can also be grown in a self-catalytic reaction, i.e., without catalyst particles (vapour-solid, VS growth).[9] The presence of a catalyst at the sample surface, however, has its advantages over the VS method as the catalyst is able to control certain

growth properties and to localize the resulting wire at a pre-defined position. The catalyst allows to grow nanowires by forming a liquid (VLS) or solid (VSS) nanoparticle in which the vaporized precursor can dissolve as can be seen in Figure 3. When passing the saturation solubility, a supersaturated state will be created upon further deposition of precursor molecules on top of the catalyst surface. This supersaturation state is energetically unfavourable resulting into the crystallization of excess precursor material at the bottom of the droplet. With still more source vapour being present in the vicinity of the catalyst particle, the supersaturated state will continue to exist leading to a continuous crystallization process and, thus, the growth of a nanowire.[9, 49]
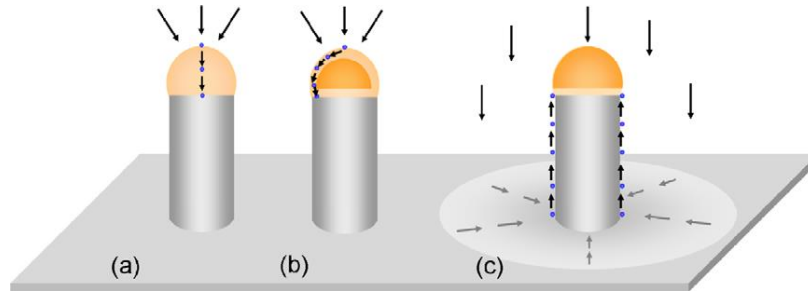

Figure 3 shows the VLS mechanism with a) a fully molten catalyst (VLS mechanism), B) a semi-molten catalyst and C) a solid catalyst (VSS mechanism)

To form tin oxide (SnO_2) nanowires by means of the VLS method different parameters need to be considered. The precursor material used to form the source vapour is one of them. Obviously, when growing SnO_2 nanowires, the precursor has to contain Sn. There are, however, different materials possible which could serve as a precursor: a pure Sn source, SnO or SnO_2 as can be seen in Table 1. Each of these materials will have different requirements in vaporization temperature and carrier gas. It will not be possible to create SnO_2 nanowires from a pure Sn source when working in a fully inert argon environment, so some oxygen has to be added to the system as well. The same holds true for the SnO source material: it does contain some oxygen, but this is not enough to form nanowires with SnO_2 stoichiometry. When using a pure SnO_2 source, additional oxygen is not needed, but to achieve a reasonable vapour pressure the temperature of the furnace has to be set to very high values as can be seen in Table 1. Here, the addition of carbon helps to reduce the growth temperature which makes the process more efficient. In general a mass ratio of 2:1 (SnO_2:C) is recommended.[50] Experimentally, the growth temperature can be lowered by admixing graphite (C) to the SnO_2 source material leading to the following carbothermal reduction reactions:[51]
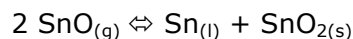
$$C_{(s)} + SnO_{2\ (s)} \Leftrightarrow SnO_{(g)} + CO_{(g)}$$

$$CO_{(g)} + SnO_{2\ (s)} \Leftrightarrow SnO_{(g)} + CO_{2(g)}$$

$$2\ SnO_{(g)} \Leftrightarrow Sn_{(l)} + SnO_{2(s)}$$

Table 1 gives a literature overview of the different conditions found to grow SnO$_2$ nanowires.

Source material	Temperature (°C)		Flow rate (sccm)	Pressure	Time (H)	Reference
	Core	Substrate				
Sn shot	900	900?	1000 ml(/h?)	?	0,5-2	[52]
SnO$_2$ + C	700	700	100	200 torr	4	[51]
Sn + O	900	?	50 ml/min	?	0,5	[53]
SnO2	1370	350-500	50-100	50-200 mbar	?	[54]
SnO + O	960	lower	50	10 torr	0,5	[55]
SnO$_2$ + C	800	?	300-500	10 torr	0,5	[56] +supplement
Sn +O	800-1000	900	100-1000	?	0,5-3	[57]
SnO$_2$ + C	800	?	300	10 torr	0,5	[50]
SnO$_2$ + C (ITO)	?	840	100	30 mbar	0,75	[58]
SnO$_2$ + C	880	?	400	?	20 min	[59]

In this work, in order to grow SnO$_2$ nanowires in a controlled way, gold nanoparticle arrays will be created first by the micellar method allowing to adjust the particle size between 1 and 10nm. Subsequently, the growth conditions need to be established for the available experimental setup. Finally, efforts will be spend to determine the relation between the catalyst particle size and the resulting diameter of the nanowires which is the key to control the physical and chemical properties of such wires in future studies.

Materials and Methods

Gold catalyst particles

Micelles

The micellar approach as described by G. Kästle et al. (2003) was used to create the gold nanoparticles as catalysts in a diameter-controlled way.[44] Briefly, 25 mg of the diblock-copolymer poly(styrene)-block-poly(2-vinylpyridine) (PS-b-P2VP) commercially available from Polymer Source, Inc. (Canada), is dissolved in 5 ml extra dry toluene (<0,003% H_2O) and stirred for a period of 3 days to form reversed micelles (as visualized in Figure 4). Varying the amount of gold salt ($HAuCl_4$ xH_2O, Sigma Aldrich) added to these solutions will determine the resulting size of the gold particles.[60, 61] The polar gold salt will diffuse through the apolar solvent toluene into the polar core of the reverse micelles resulting in the protonation of the ring nitrogen in the P2VP part (Figure 5). According to literature the maximum amount of metal salt which can reliably be added must not exceed a loading ratio of 0.5 (metal ions versus pyridine groups).[44, 61] The amount of Au salt to be added at a given loading ratio can be calculated according to the formula below:

$$x = \frac{mass\ of\ polymer}{M_{PS} + M_{P2VP}} \times \frac{M_{W(P2VP)}}{M_{C_7H_7N}} \times loading\ factor \times M_{gold\ salt}$$
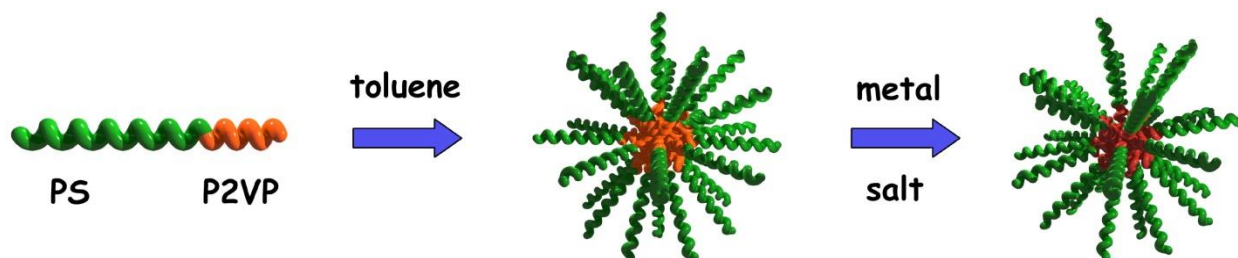

Figure 4 illustrates schematically how the block-copolymer strands form a reverse micelle that can be loaded with the metal salt.
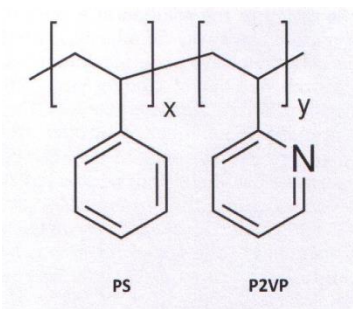
Figure 5 represents the structural formula of the PS-P2VP polymer.

Next to the amount of metal salt added to a micellar solution, the resulting particle size can also be tuned by changing the length of the polar P2VP block. Furthermore, increasing the length of the apolar PS part will increase the steric hindrance between the micelles and, thus, their diameter in solution which controls the final center-to-center distance between them after their deposition as mono-micellar film on a substrate. Two different PS/P2VP

ratios where used for the creation of the micelles as can be seen in Table 2. For the creation of smaller particles (± 3nm) the 325/78 polymer works best while for the creation of the larger particles (± 9 nm) the 1850/900 polymer works best.

Table 2 shows the polymer short name and the mass distribution of the polymer into its different compounds as well as the usual dipping speed.

Short name	M_{PS} (g/mol)	M_{P2VP} (g/mol)	Dip speed (mm/min)
325/78	32500	7800	3,5 – 6
1850/900	185000	90000	14 – 15

A second method, that is very effective in the creation of the smaller particles uses ultrasound (US) for 2 hours to dissolve the PS-P2VP and gold salt both at once (for a detailed protocol see supplement1).

Transformation of micelles into particles

Sample preperation
A 380 µm thick n-type silicon (100) wafer doped with phosphorus (crystec kristalltechnologie) is cut into samples (1 x 0,5 cm) with a diamond cutter. The cut samples are placed in isopropanol and ultrasonicated for at least 10 minutes before changing the washing medium to acetone and ultrasonicated for another 10 minutes. This washing cycle is repeated twice. Before storing the cleaned substrates, one additional ultrasound cleaning step in Demi water is performed for a minimum of 10 minutes after which each sample is dried with nitrogen.

Sample loading
The cleaned substrates are then used for dip coating the solutions. The speed at which the home made dip coater can be varied, ranges between 1 and at least 22 mm/min by changing the voltage applied to the electrical stepper motor as can be seen in Figure 6. The optimum dip speed depends on the size of the micelles in solution and an indication of the optimum speed for the used polymers is shown in Table 2. The samples are dipped into the solution at a constant speed and just before the solution level reaches the sample holder the voltage to the motor is reversed allowing to pull the substrate out of the solution at the same constant speed. After its complete pulling-out of the micellar solution, the sample is left hanging on the holder inside the flask in order to fully dry from the toluene before further retrieval of the sample. This process is illustrated in the left and top part of Figure 7.
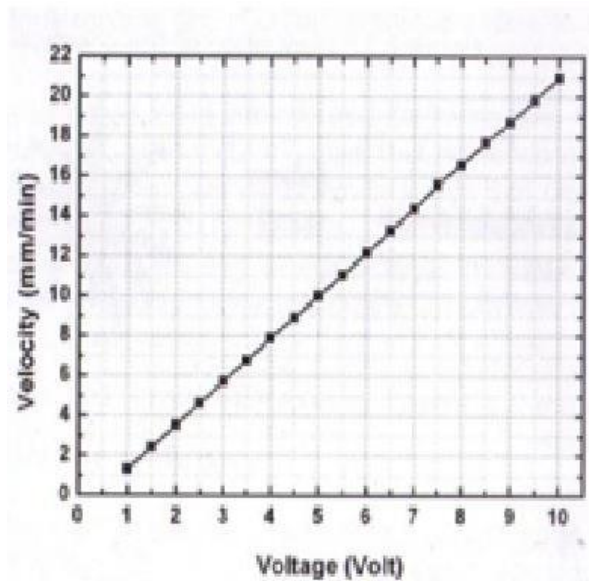
Figure 6 shows the relation between the applied voltage and the dip coating speed.
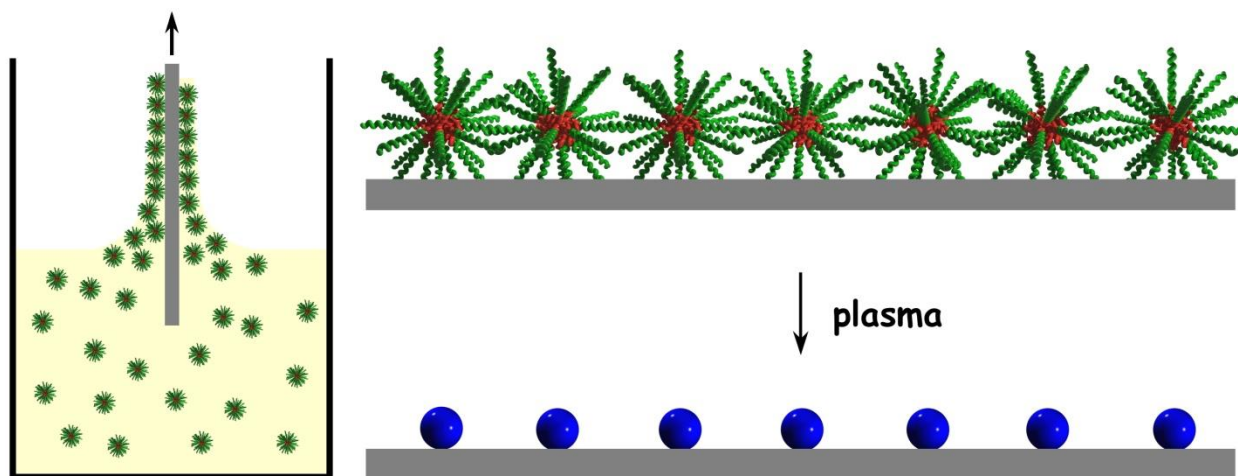

Figure 7 sketch of the dip coating and plasma treatment. It shows how the micelles attach to the surface of the silicon substrate to form a uniform monolayer that leaves the gold particles after plasma treatment.

After dip coating the samples can be checked by Atomic Force Microscopy (AFM, Park-NX10) in non-contact mode and X-ray photoelectron spectroscopy (XPS) (1486.6eV, Al-K$_\alpha$) to determine the morphology and its composition, respectively. When the sample is of good quality a uniform hexagonally-organized monolayer of salt-loaded micelles can be seen in AFM and more samples are taken from the solution for further use. If the quality is low one could either try to take a new sample at a different dipping speed or stir the solution for another week, after which a new sample will be taken to check the quality of the solution.

Catalyst preparation
To completely remove the polymers involved, an oxygen plasma is applied to the micellar monolayer on top of the Si substrates. The samples are placed inside a commercial plasma system (Technicus PDII-A) and the chamber is evacuated down to a pressure of ~0,1 mbar

before oxygen is provided to the plasma chamber at a flow of 35 sccm. For the 325/78 polymer 50 watt plasma is applied for 30 minutes at room temperature while for the 1850/900 polymer 20 watt plasma is used at 250 °C for 30 minutes (illustrated in the bottom part of Figure 7). The system is water cooled during the etching cycle to prevent damage to the rf-electrode samples and the system itself. After the samples have cooled down they can be stored in ambient conditions during which the gold oxide will reduce to gold or if needed directly placed in ethanol for 5 minutes to fasten the process. The samples will then be checked again for morphology and composition by AFM and XPS respectively.

Analysis

The AFM images are flattened by the AFM software (Park System, XEI) and further processed with Gwyddion (V2.29).[62] The scan image is levelled at its medium and recalibrated to zero before a mask is applied to capture the size distribution of the particles. Next, a 2D statistical auto covariance function is calculated allowing to determine the inter-particle distance

The data from Gwyddion is than imported into OriginPro (V8.6, OriginLab, Northampton) with some home written scripts that directly calculate the particle size and inter-particle distance while graphically visualizing the data (a copy of the import scripts can be found in supplement2).
For the XPS data no import script has been written, but the graphs were also made in origin and manually analyzed with the aid of the Handbooks of Monochromatic XPS Spectra.[63]

Growing nanowires

The nanowires are grown in a horizontal double tube system as has been described by C. Geng et al. (2004) for ZnO nanowires.[64] In the master project the double tube system as sketched in Figure 8 was used to grow SnO_2 nanowires. The outer quartz tube has a inner diameter of 7,3 cm and a length of 125 cm, the inner semi-closed quartz tube ('inliner') has an inner diameter of 5,5 cm and a length of 25 cm. The sample substrates are placed on the centre of a circular ceramic disk (diameter of 2,2 cm and a height of 0,4 cm) at the positions 1, 2, 3, 4 and 5 with a centre to centre distance of 4 cm between the positions. Positions 1 – 3 are drawn into Figure 8, while positions 4 and 5 are closer towards the centre of the oven. At all positions, the discs are elevated on a ceramic holder with a height of 1,8 cm to get closer to the vapor source. Positions 4 and 5 can be created on different ways, either by keeping the inliner at the same place and moving the ceramic holder with 4 and 8 cm respectively closer to the growth precursor (moving holder). Alternatively, the distance between the growth precursor and the sample substrate inside the inliner is kept constant while the entire inliner is moved over a distance of 4 or 8 cm, respectively, into the oven (moving inliner).

Temperature calibration

The double tube system is placed inside a horizontal tube furnace (carbolite, analis) for the nanowire growth. To get an insight into the temperature at the substrate positions a single tube setup was used in combination with 4 metals with known melting temperatures namely: highly pure indium (99,999%; Johnson Matthey Alfa Products; 156 °C), soldering tin (Sn99,3/Cu0,7; Felder; 227 °C), roofing lead (1 mm; 327 °C) and aluminum (99%; 1 mm; 665 °C). From each of these metals at least three small pieces where cut and placed

on clean silicon samples. the sample where positioned on an elevated ceramic holder to have a certain distance from the outside of the insulation layer (Figure 8). This distance was varied between the different heat runs to get a first approximation. The distance was than optimized by using 3 samples per metal with a separation of 0,5 cm around the position found form the first approximation. After placing the holder into the furnace the temperature is ramped up with 28 °C/min (using a Eurotherm type 818 temperature control unit) to the working temperature of 1000 ± 4 °C during which Ar gas (purity 6N, Alphagaz) is continually flown into the system at 100 sccm. The working temperature is kept constant for 30 minutes after which is determined up to what position the metals did melt. When all 3 metals of the fine tune distance melted or non the run was repeated and the distance changed accordingly. From these experiments the temperature profile of the oven can be determined.
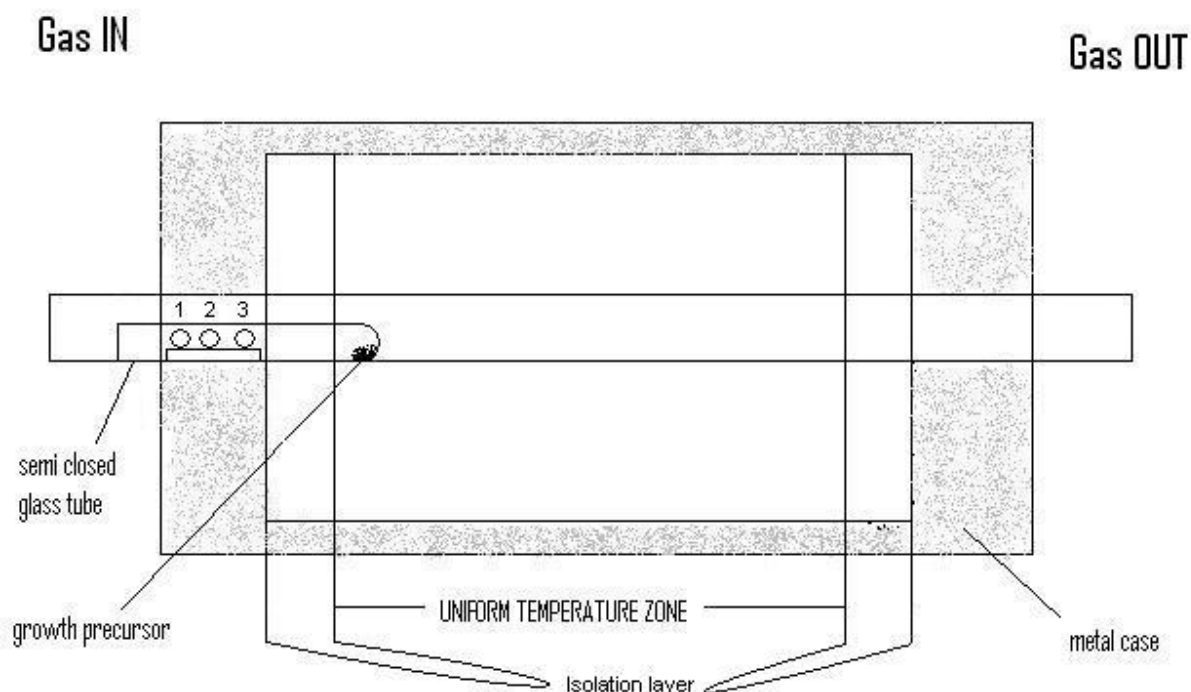

Figure 8 represents a sketch of the double tube system that was used for the growth of the nanowires. The main gas flow is reversed compared to the relative positions of the substrates and the precursor. The semi-close inliner changes the flow from precursor to source into the main gas flow. The positions 1,2 and 3 indicate the initial growth positions used for the growth and are separated approximately 4 cm from each other (centre to centre).

Growing wires

With the temperature profile of the oven known, the growth of nanowires will now be investigated. All growth cycles make use of the carbothermal reduction reaction with SnO_2 (Strem Chemicals 99,9%) and graphite (Alfa Aeser, 99,9999%) as the source materials[51]. Before every reaction the SnO_2 and graphite powders where mixed together in a 2:1 (respectively) weight ratio to a total mass of 0,75 g and placed near the closed side of the inliner tube. The samples with gold catalyst where placed near the open end of the inliner

on the ceramic disks on top of the holder. This setup was loaded into the larger quartz tube and positioned so that the samples would be at the correct positions as indicated in Figure 8. After loading the larger quartz tube was closed at both ends with metal caps and the tube was evacuated to approximately 10 mbar. The system was than filled with highly pure Ar gas that has an overpressure of approximately 50 mbar with respect to the ambient air. The filled system was closed and the overpressure was released in the ambient before setting the desired flow rate.

A detailed analysis was preformed to find the optimum growth conditions as indicated below, where the starting values were taken from a pilot study (core 1000 °C, growth at position 2 or 3, flow rate 100 sccm, time 2h and samples with 3 nm gold catalyst particles), as soon as better conditions were found the latter were used in subsequent experiments .

Temperature

There are two temperatures that influence the growth of the wires, first the core temperature of the furnace (which affects the evaporation of the source material), and secondly the temperature of the nanoparticle samples. A systematic approach was used to narrow down the best temperatures of growth. The different core temperatures were selected based on literature (Table 1) and growth was performed on positions known to work from a pilot study (positions 2 and 3). The used core temperatures varied between 700 and 1100 °C as indicated in Table 3. After setting the optimum core temperature the growth temperature was varied by choosing five different growth positions of which three are indicated in Figure 8. The two remaining positions (4 and 5) are created as was discussed above. Table 4 shows the different trails undertaken to find best position for the nanowires to grow.

Table 3 shows the different core temperatures that were tested for the nano wire growth. The runs with core temperature of 950 and 1050 °C were used to fine-tune. The positions marked in yellow are created by moving the inliner tube.

Core temperature (°C)	Position				
	1	2	3	4	5
700		x	x		
900		x	x		
950			x	x	
1000	x	x	x		
1050			x	x	
1100		x	x		

Table 4 shows the positions used to place the samples. The positions marked in yellow are created by moving the inliner, while the positions marked in red are created by moving the substrate holder inside the inliner. The trail marked with both yellow and red is created by moving both, the inliner and the holder, by one position.

Core temperature (°C)	Position				
	1	2	3	4	5
1000	x	x	x		
1000		x	x	x	
1000		x	x	x	
1000			x	x	X
1000			x	x	X
1000			x	x	X

Gas flow
Literature reports different flow rates for the growth of nanowires as indicated in Table 1. Five different flow rates between 0 and 300 sccm were tested. Attention has to be paid to the flow direction of the experiments, compared to the main gas flow the samples are placed up stream of the source. The flow rate was set with a flow meter (Dwyer, VFA-visi-Float) and kept constant during a full growth cycle.

Growth time
The length of the nanowires depends on how long the wires are allowed to grow. To get an insight into this effect nanowires where allowed to grow for 0,5 min, 5 min, 10 min, 15 min, 30 min, 1 h and 2 h.

Diameter control
After having the growth process fully optimized a multi batch experiment was performed with different sizes of the catalyst particles to investigate the ability to control the diameter of the wires. The samples were all placed on the circular ceramic disc that itself was placed at position 3½. This experiment was performed under the optimum growth conditions determined in the experiments mentioned before.

Supplementary experiments
To further study the alignment of the nanowires a silicon substrate was covered with a thin layer of Al_2O_3 (prepared by sputtering) before the deposition of the catalyst particle array. Subsequently, nanowires were grown on positions 3, 4 and 5.

Analysis
All samples were routinely analyzed by field emission scanning electron microscopy (FE-SEM, Philips FEI Quanta 200-FEG) with a minimum magnification of 10.000X to screen for the successful growth of the nanowires and the morphology of the wires. Higher magnifications up to 200.000X were applied for further analysis and to determine the diameter of the grown wires. The diameter was determined using the ImageJ software.[65] Here, the scale bar present in each image was measured by the software to define its length scale. Hereafter, multiple line profiles where taken parallel over the wire to measure its cross section. The individual diameter is then exported to Origin to calculate an average value and the corresponding standard deviation of the sample.

Some samples were additionally investigated by Raman spectrometry (Jobin-Yvon T64000) using a 488 nm laser (Lexel SHG-95) as excitation source to determine the material properties of the sample. Furthermore, some samples were also investigated by AFM to provide height profiles of the wires.

Results & discussion

Gold catalyst particles

AFM of micelles

Dip coating was performed on 18 different micellar solutions: of these solutions, 10 were made with the 325/78 copolymer (called 'short polymers' hereafter) of which two were prepared using ultrasonication (US) and 8 solutions were made with the 1850/900 copolymer (called 'long polymers' hereafter). No solution was synthesized with the US for the long polymer, because of the low quality of the samples resulting from this protocol. When using the US protocol the short polymer micelles form in a fast way and the array quality is about the same as for a solution made by stirring as can be seen in Figure 9. The image on the left side (A) shows the US protocol while the image on the right side (B) is taken from a solution made by the conventional stirring method. From these image the average height of the micelles can be calculated for the US protocol and the conventional method and shows little difference between both approaches with values of 11,59 ± 1,32 and 12,78 ± 1,29 nm, respectively, as also can be inferred from the height distribution plots in the bottom of Figure 9 (C & D). The inserts in Figure 9A and B represent the 2D autocorrelation that reveal the hexagonal order of the sample from which the inter-particle distance can be calculated. From these calculations it is found that the inter-particle distance for the US protocol is 44,59 ± 2,07 nm and for the conventional stirring the distance is 40,21 ± 2,13 nm which are both comparable within the error bar. Small differences can be seen in the degree of hexagonal short range order which indicates a slightly better order for the conventional method. To create a solution on a short time frame the US protocol works good however reusing this solution 5 days later will not give equal results anymore as the order of the solution has decrease as can be seen in Figure 10.
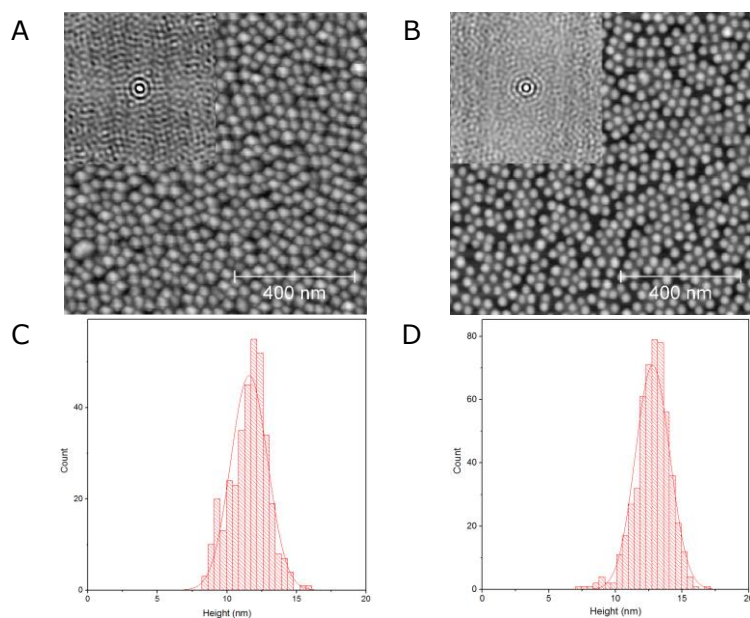

Figure 9: AFM images of the fast US protocol (A) and the conventional stirring protocoll (B). The insets on the top left represent the autocorrelation function of the images from which the degree of hexagonal order can be judged. Graph C represents the corresponding height distriubtions.
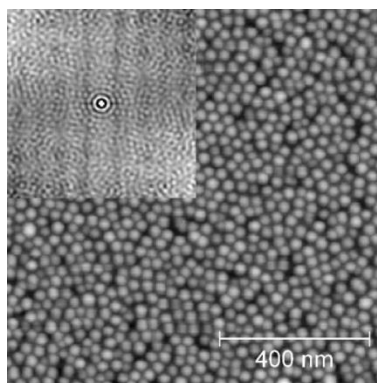
Figure 10 shows the AFM image of the US solution after 5 days of stirring with in the top left the autocorrelation insert that shows a limited degree of hexagonal order.

A monolayer of salt-loaded long polymer micelle has an average height of 31,24 ± 2,06 nm as can be seen from the size distribution in the right of Figure 11. The array is of higher quality than in case of micelles derived from the short copolymers possibly due to a better distribution in chain length (polydispersity index).
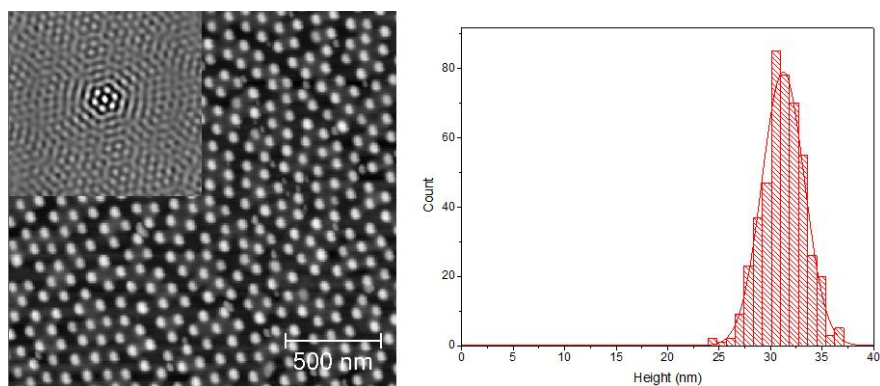

Figure 11 shows an AFM image of the long copolymer-based gold salt-loaded micelles including its autocorrelation function as inset, together with the corresponding height histogram

From micelles to particles followed by XPS

The micelles themselves are burned off with oxygen plasma in order to arrive at an array of nanoparticles. This etching step can be followed up with two XPS measurements, one performed before etching and one after polymer removal as shown in Figure 12. In this figure the red line corresponds to gold nanoparticles and the black line to micelles on a Si substrate. The peak in the XPS spectrum of the micelles that is related to the organic material (C1s) has disappeared after etching thereby indicating that the organic compound is no longer present after plasma treatment. Some new peaks appear after polymer removal, which correspond to Au core levels. Remarkable is the peak at 1070 eV representing Na1s, which is not present in the elemental distribution neither of the substrate nor of the salt-loaded micelles. This peak rather reflects a cross-contamination arising from the sample holder.
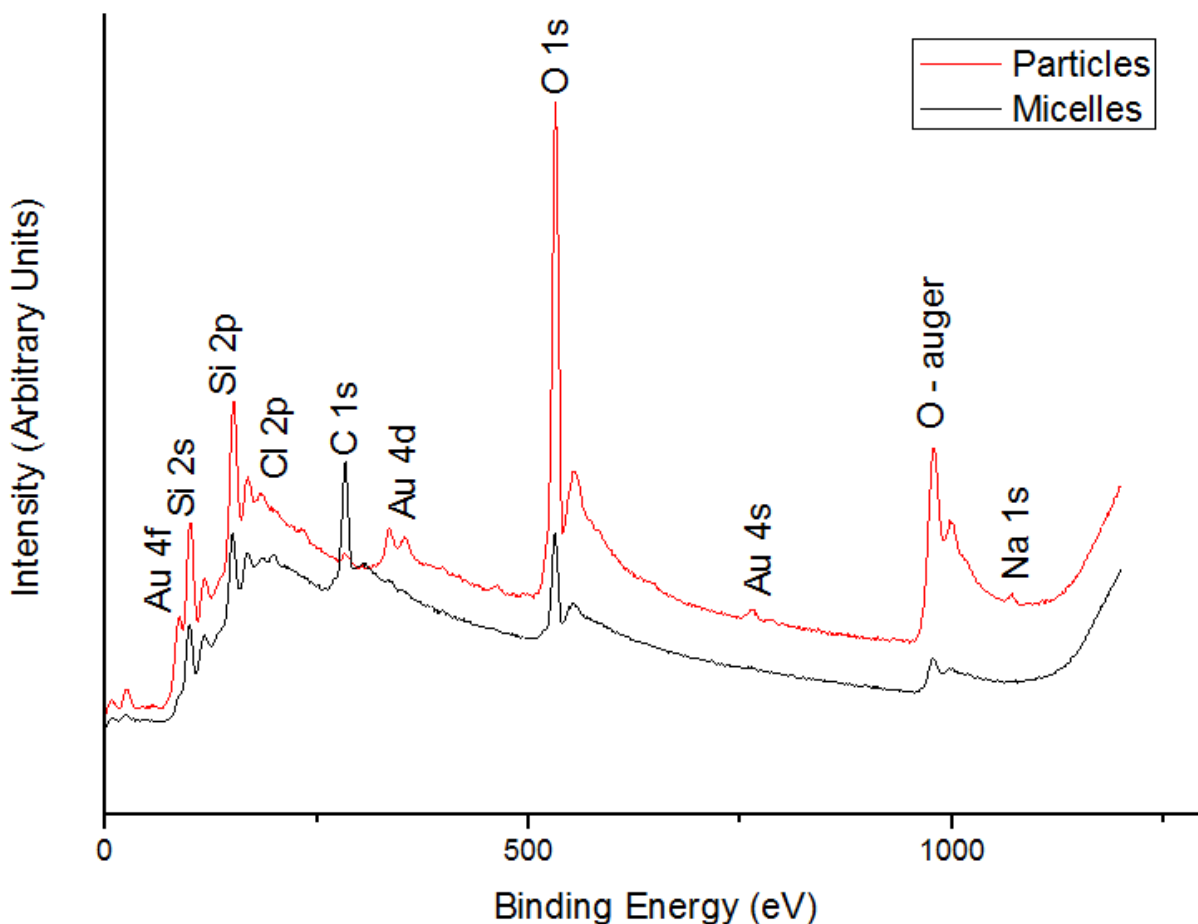
22

Figure 12 shows the XPS spectrum for both the micelles (black) and the raw gold particles (red). It can be seen that some of the peaks that are present before the plasma treatment have disappeared and some other gold specific peaks appear.

AFM of particles

After plasma etching, the sample contains basically gold and silicon/silicon oxide as shown by XPS. This can also be proven by looking at the average particle height before and after plasma etching. Figure 13 shows an AFM scan taken after plasma etching of a small polymer micelle made by conventional stirring. The particle size has drastically changed as evidenced by an average size of 2,68 ± 0,24 nm which is derived from the height histogram on the right side of the figure. By comparing the height of the particles before (12,78 nm) and after (2,68 nm) etching, additional evidence (besides the XPS results) is found that the micelles were successfully removed leaving bare gold particles at the substrate surface. The inter-particle distance (39,79 ± 1,42 nm) of this AFM scan (calculated from the autocorrelation function shown as inset) has not changed significantly compared to the AFM scan performed on the corresponding micellar array (Figure 9B).
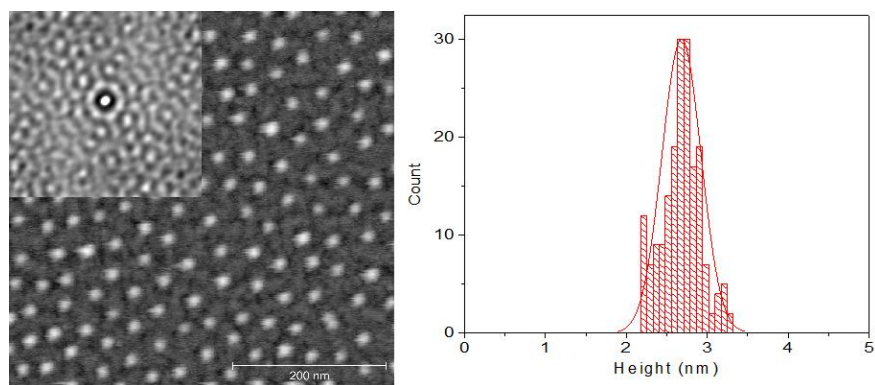
Figure 13: AFM image (left) and height distribution (right) of gold nanoparticles with an average diameter of 2,68 nm. The inset on the left side represents the autocorrelation function of the image which shows a reasonable hexagonal patron.

A large change in height upon plasma treatment is also found for the long polymer micelles. Here, decrease form 31,24 nm before etching to a average height of 7,76 ± 0,69 nm after etching is observed as derived from the height distribution on the right side of Figure 14. As has already been shown before, the hexagonal order of the long polymer micellar arrays was better than for the short polymer-based micellar ensembles. This also holds true for the resulting gold particle arrays that are created after etching a sample with a long polymer micelle array as can be inferred from the autocorrelation function presented in Figure 14.
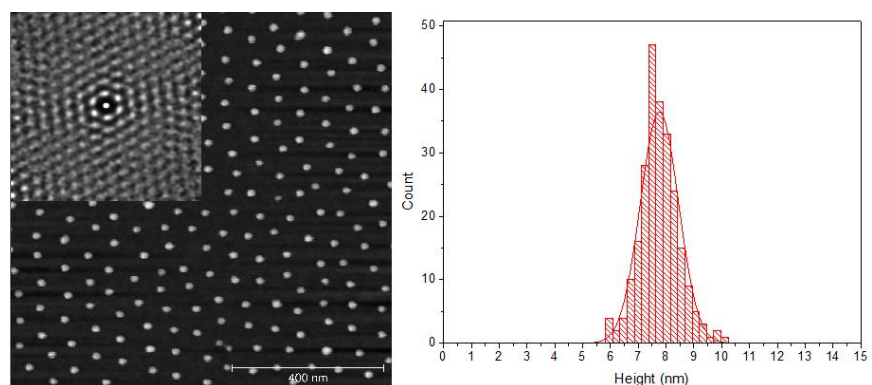

Figure 14 shows an AFM image of particles made from the long copolymer with a size of 7,76 nm as can be seen in the size distribution on the right side.

The maximum particle size these micelles allow to prepare depends on the loading ratio (ratio between metal ions and pyridine groups) or the amount of metal salt added to the solution. The maximum loading ratio that will create stable micelles is 0,5 and when using this ratio for a long polymer micelle this lead to the creation of a maximum average height of 10,44 ± 1,28 nm and a maximum average height of 5,5 ± 0,4 nm for particles made from the short polymer. Decreasing this loading ratio will decrease the particle size as has been reported by G. Kästle et al.[44] Such a behaviour can be seen in Figure 15 where the black symbols represent solutions made with the short polymer and the red symbols represent the solutions made with the long polymer. The blue and yellow symbols both represent micellar solutions based on short and long polymers, respectively, to which some additional gold salt was added every week thus increasing their loading ratios. Three days

24

after adding the additional salt, the samples were dip coated from the solution and scanned by AFM. From the graph it can be seen that the loading ratio and the particles size have a non-linear relation. An increase in the loading of the micelles will lead to a similar increase in the volume of the resulting particles. As the radius of a particle has a cubic relation to its volume, a third root (i.e. non-linear) dependence of the particle size on loading ratio is expected for the individual data sets presented in Figure 15 especially when taking into account that a loading ratio of 0 will create a particle with size 0.
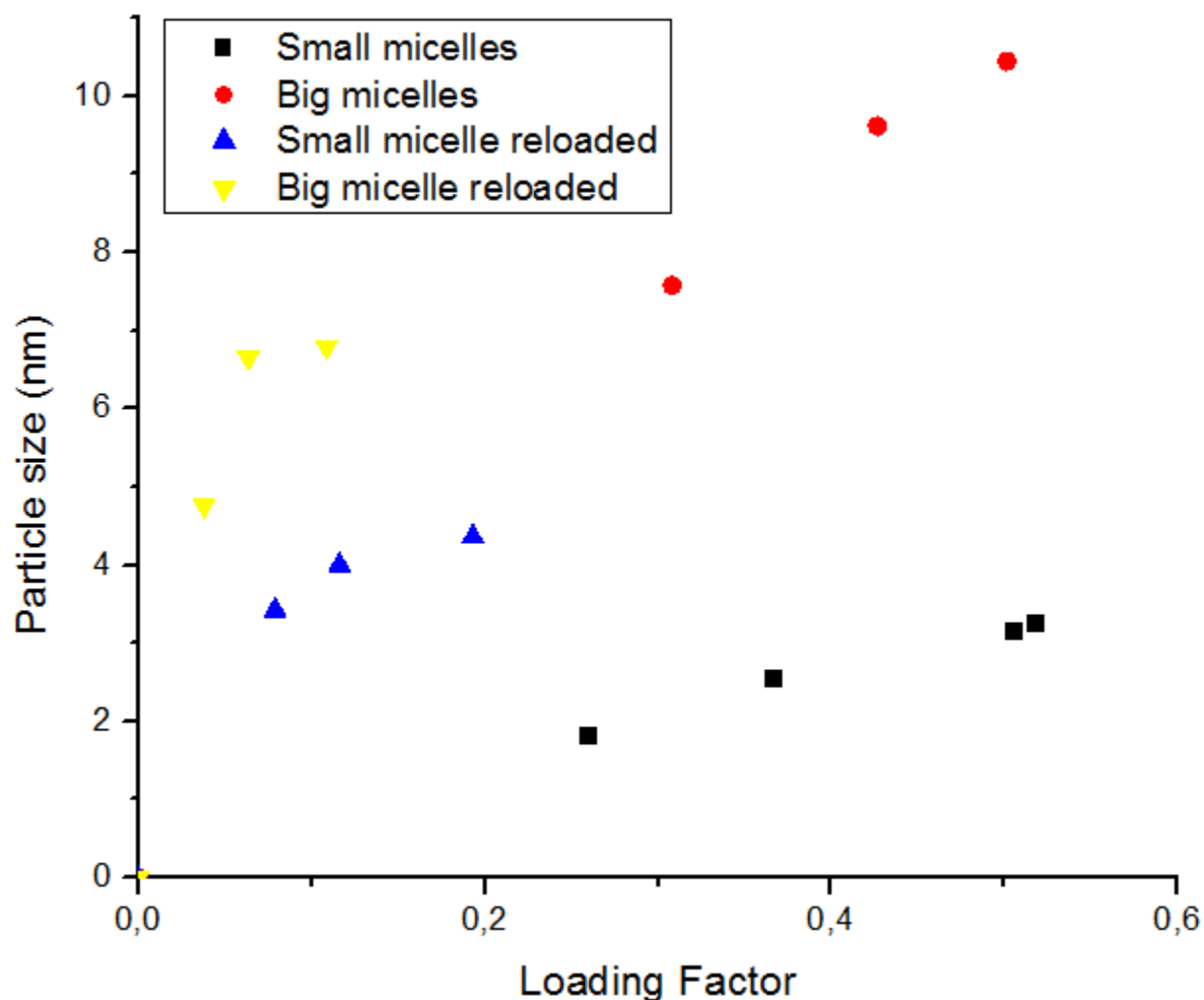

Figure 15 represent a graph of all different solutions made with their respected loading of gold salt and the particles size after etching.

Wetting problem

On some of the SEM images taken after nanowire deposition, inconsistencies in the growth density of the nanowires was observed. Two possible reasons causing this problem were envisaged. One was that the underlying nanoparticles where not well distributed, the other one suggested fluctuations in the flow rate of the carrier gas creating wave patterns on the substrate (as will be discussed in supplement 3).

The idea in which density fluctuations observed sometimes within nanowire ensembles might be the result of density fluctuations within the underlying array of catalyst particles was investigated by taking a large AFM scan of 20 X 20 µm as is shown in Figure 16. Here, a clear difference in the density of the gold catalyst particles is seen arising from a non-homogeneous wetting of the substrate during the dip-coating process. The magnified region represents a 1x1 µm scan that is normally taken to determine the particle size and its distribution. Obviously, micelles must have been deposited in a rather inhomogeneous way reflecting a local wetting contrast for toluene on the Si substrate.
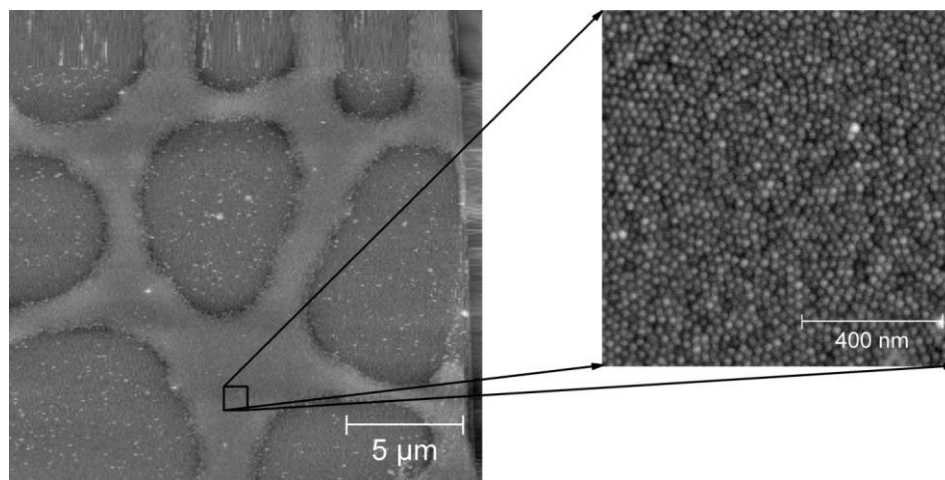

Figure 16 shows a 20 x 20 µm scan size on the left that clearly indicates a wetting problem during the deposition of the micellar solution.

This was surprising as pre-determined dip coating velocities were used that showed good wetting abilities for such type of samples in the past. To increase the surface coverage of the gold particle array, the speed during dip-coating was varied and the results are shown in Figure 17. From this series of images it becomes clear that, with higher dipping speed, the array quality is increased. However, no wetting problem was detected on larger scan sizes for all 3 dipping velocities on those samples thus ruling out an incorrect speed for the samples showing the wetting problem as demonstrated in Figure 16. Thus, contaminations on the substrate surface possibly induced by cleaning procedures might cause this problem.
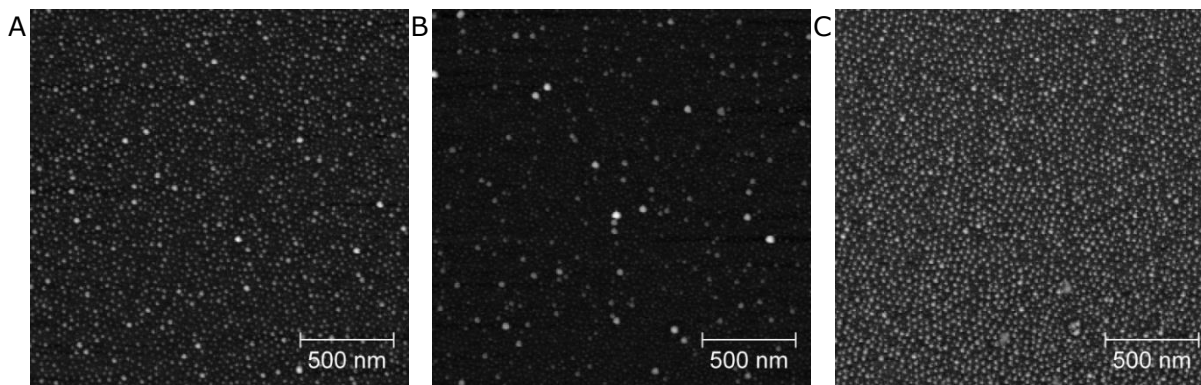

Figure 17 shows AFM images of samples prepared by increasing dipping speeds: Sample A was dipped at 5,75 mm/min, B at 8 mm/min and C at 10 mm/min.

SnO₂ particles

Besides the usual loading with Gold salt an attempt was also made to load micelles directly with the precursor material used to grow the nanowires. Thus micelles where loaded with SnO_2 that was first dissolved in methanol before adding to the micellar solution. The resulting micelles can be imaged by AFM (Figure 18, left side). However, after plasma etching, no particles are detected (Figure 18, right side) thus evidencing the presence of empty micelles after 'salt loading' in this case.
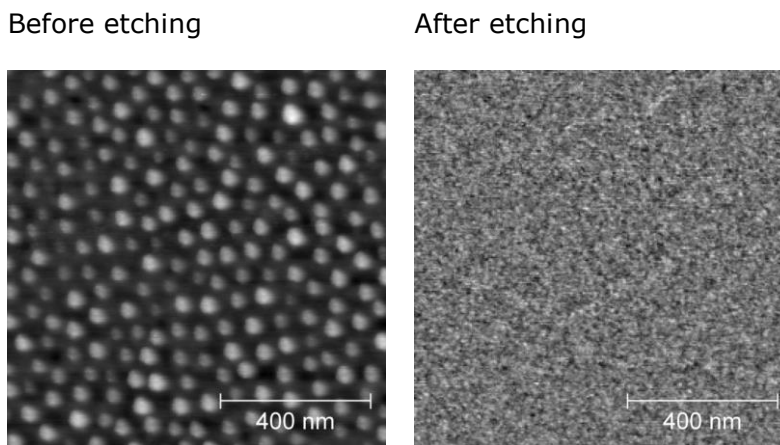
Before etching   After etching

Figure 18 shows the AFM images from the SnO2 loaded micelles before and after etching. It can be seen that the micelles are present however after removing the organic micelles nothing remains on the surface of the sample and no particles have formed.

Growth of SnO₂ nanowires

Growth temperature

In order to optimize the growth of nanowires, in a first step, the core temperature was altered to find the correct value for an optimized evaporation of the source material. Simultaneously, the position of the catalyst-covered substrates was changed independently to find the best position. The corresponding SEM results (all acquired at a magnification of 200.000X) are presented in Table 7 where the positions are drawn horizontally and the different core temperatures vertically. Depending on the combination of core temperature and sample position, a variety of morphologies can be detected ranging from the presence of larger aggregates to a complete absence of any additional material (beside the catalyst particles). However, at an evaporation (core) temperature of 1000 ˚C, clear indication for nanowire growth is obtained at positions P3 and P4. Therefore, 1000 °C was chosen as optimum temperature for nanowire growth at positions between P3 and P4. Using the temperature calibration as described below, the deposition temperature can be adjusted between 628 °C (at P4) and 482 ˚C (at P3), which seems to be on the low growth temperature side compared to other reports in the literature (Table 1)[51, 58].

Table 5 SEM images acquired after growth of nanowires at different core temperatures ranging between 700 and 1100 ˚C and at different growth positions (P2-5)

Position / Temp ˚C	P2	P3	P4	P5
700				
900				
950				
1000				
1050				
1100				

Temperature calibration of tubular furnace

The core temperature of the oven is directly registered by a thermocouple that is built into the furnace and feeds back to the temperature control unit. This temperature is defined only within the uniform temperature zone of the furnace as indicated in Figure 8. Outside this zone, the temperature decreases with increasing distance from the zone boundaries. The nanowires tend to grow outside the uniform zone at a lower temperature. After adjusting the core temperature of the furnace to 1000°C, this lower temperature is estimated by the known melting temperatures of certain metals which are placed at various positions in the vicinity of the end position of the isolation layer (see Figure 19, upper part). A linear fit to the data yields an intercept of 482 °C (corresponding to the end position of the isolation layer) and a slope of -36,6 °C/cm, thus allowing to estimate the growth temperature when placing the catalyst-covered substrate within the growth zone.
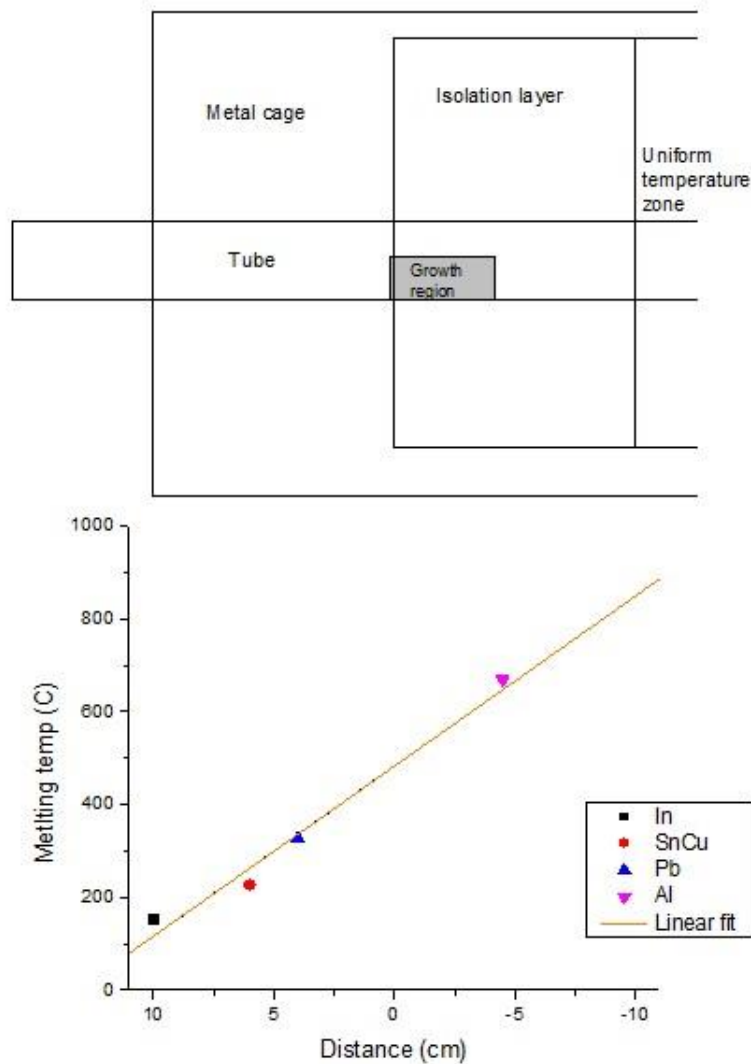

Figure 19 shows the temperature profile of the furnace outside the uniform temperature zone based on known melting temperatures of different metals (core temperature set to 1000 °C). The linear fit shows a Y-intercept of 482°C and a slope of -36,6 °C/cm.

Moving holder *vs.* moving inliner

The realization of position P4 is possible by two ways as was indicated before, by moving the sample holder leading to a change in condensation temperature and distance to the source powder or by moving the inliner only leading to a change in condensation temperature. The additional change in distance to the source powder does show an increased condensation at P4 as evidenced by Table 6. This is an empirical observation which depends on the details of the carrier gas flow within the inliner tube which could not be analyzed in more details within the time frame of this master thesis.

Table 6 visualizes the differences between the growth position P3 realized by either moving the sample holder closer to the precursor source or by moving the whole inliner tube thereby keeping the distance between sample and source material constant.
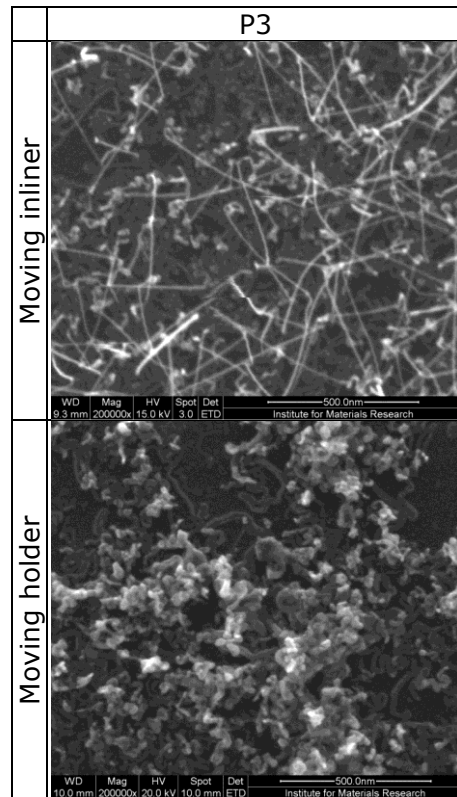
Impact of the gas flow

With both, the core temperature and the sample position optimized towards a high yield of nanowires, the influence of the flow rate is investigated as a next step. Five independent growth runs were performed at Ar flow rates of 0, 50, 100, 200 and 300 sccm. The corresponding samples where analysed by SEM and the results are summarized in Table 7. Obviously, there is a strong dependence of the growth mode on carrier gas flow as different deposition results are observed spanning again a broad range of morphologies from a complete absence of wires to worm-, pillar-, or droplet-like structures and mixtures of them. Excellent nanowires growth can be detected at position P4 only, thus evidencing the existence of rather narrow parameter windows with the flow rate of the carrier gas being one of the critical ones.

Table 7 illustrates the SEM images acquired from samples grown at different Ar flow rates (0, 50 , 100, 200 and 300 sccm) at positions P3 and P4

	P3	P4
0		
50		
100		
200		
300		
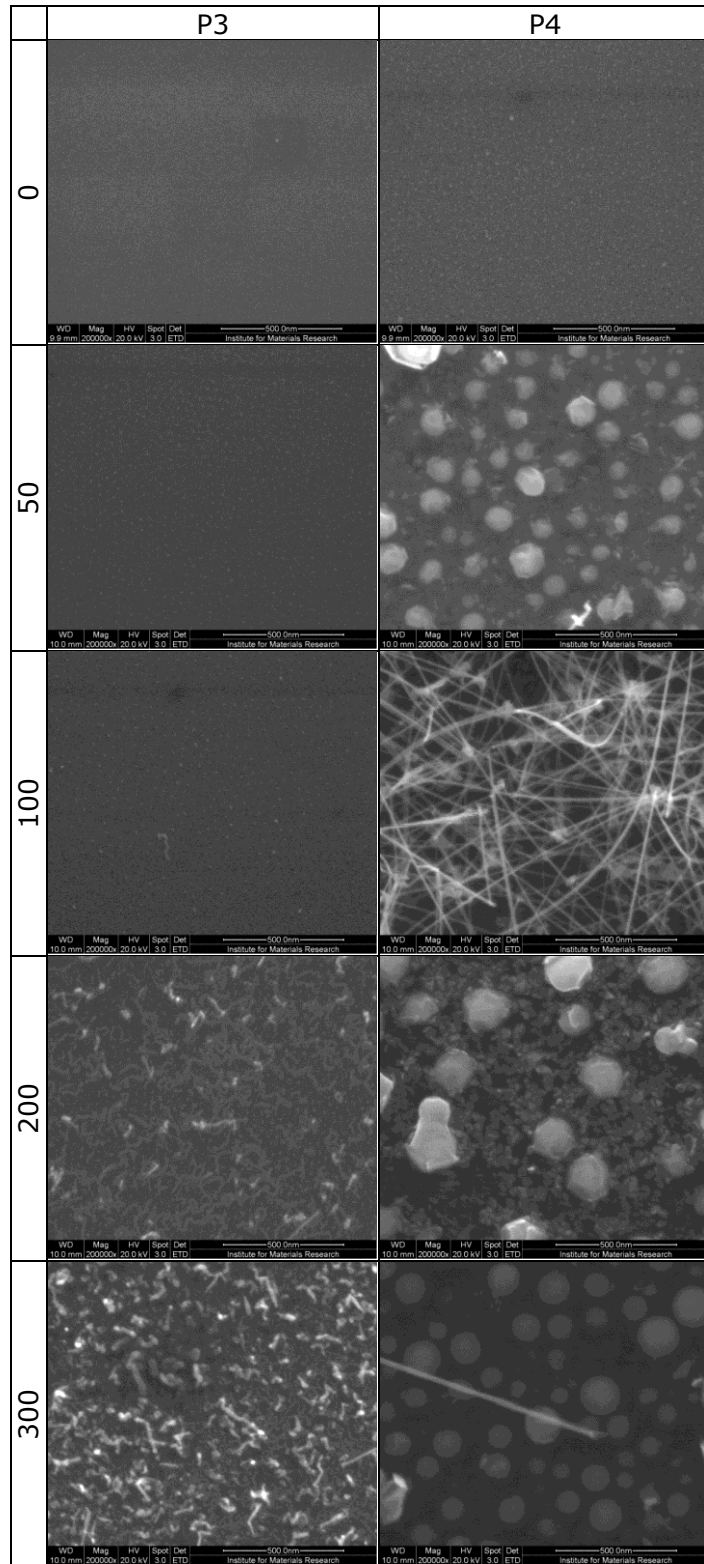
Reverse direction

One additional try was given to mimic the general experiments reported in literature with the sample lying downstream of the source material. This experiment was performed by placing the inliner at the out flow side of the furnace (core temp 1000 $^\circ$C and flow rate of 100 sccm). The result were not promising as clear indications for nanowire growth could not be obtained thus forcing to skip this direction due to the time limitation of this thesis work.

Growth time

The nanowires start to grow almost immediately once the furnace reaches 1000 $^\circ$C and most likely not before as can be determined from Figure 20A which shows the initial phase of formation. The furnace was turned off only 30 seconds after the core temperature has reached 1000 $^\circ$C. Clearly, short nanowires are detectable with an admixtures of larger objects having a cubic structure. The latter could either be contaminations on the sample or some crystalline tin structures that form initially upon reaching the evaporation temperature. Figure 20B shows an image that is created after growing for 1 H, a less dense region is shown to better illustrate the full length of the wires.
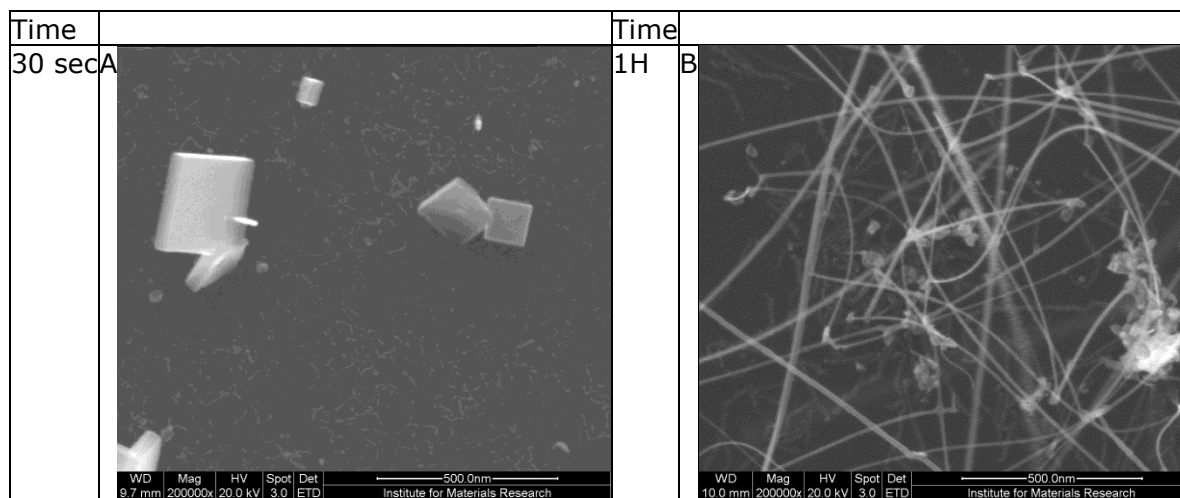

Time		Time	
30 sec A		1H B	

Figure 20 shows that the nanowires start to form almost directly after the core reaches 1000 $^\circ$C (A) where the furnace is shut down after 30 seconds. When turning of the oven after 1 hour the nanowires have increase significantly in length as is to be seen in (B).

Substrate and catalyst

The method used here was reported in the literature to allow a catalyst-free ('self-catalytic') synthesis of nanowires.[64] Furthermore, the growth of 1D nanostructures has been reported to depend on the substrate material as well (add reference). To investigate such kind of effects, an experiment with 3 different types of substrates was performed including a Si substrate with Au nanoparticles as catalyst, a Si substrate without a catalyst and a silicon substrate with a 20 nm thick Al_2O_3 film supporting the Au catalyst particles. The corresponding SEM images, taken after growth, are presented in Figure 21 were a clear difference can be observed between the Al_2O_3 substrate and the silicon substrate both hosting Au particles as catalysts.

The Al_2O_3 substrate forms a less dense coverage of nanowires as compared to the pure Si substrate as observed at both magnifications. It also tends to form additional structures next to the nanowires. In contrast, the silicon substrate allows a more uniform coverage of

nanowires grown from Au nanoparticles. In case of the catalyst-free Si substrate, no evidence for the existence of nanowires is found thus ruling out an auto-catalytic growth of nanowires on top of our substrates.
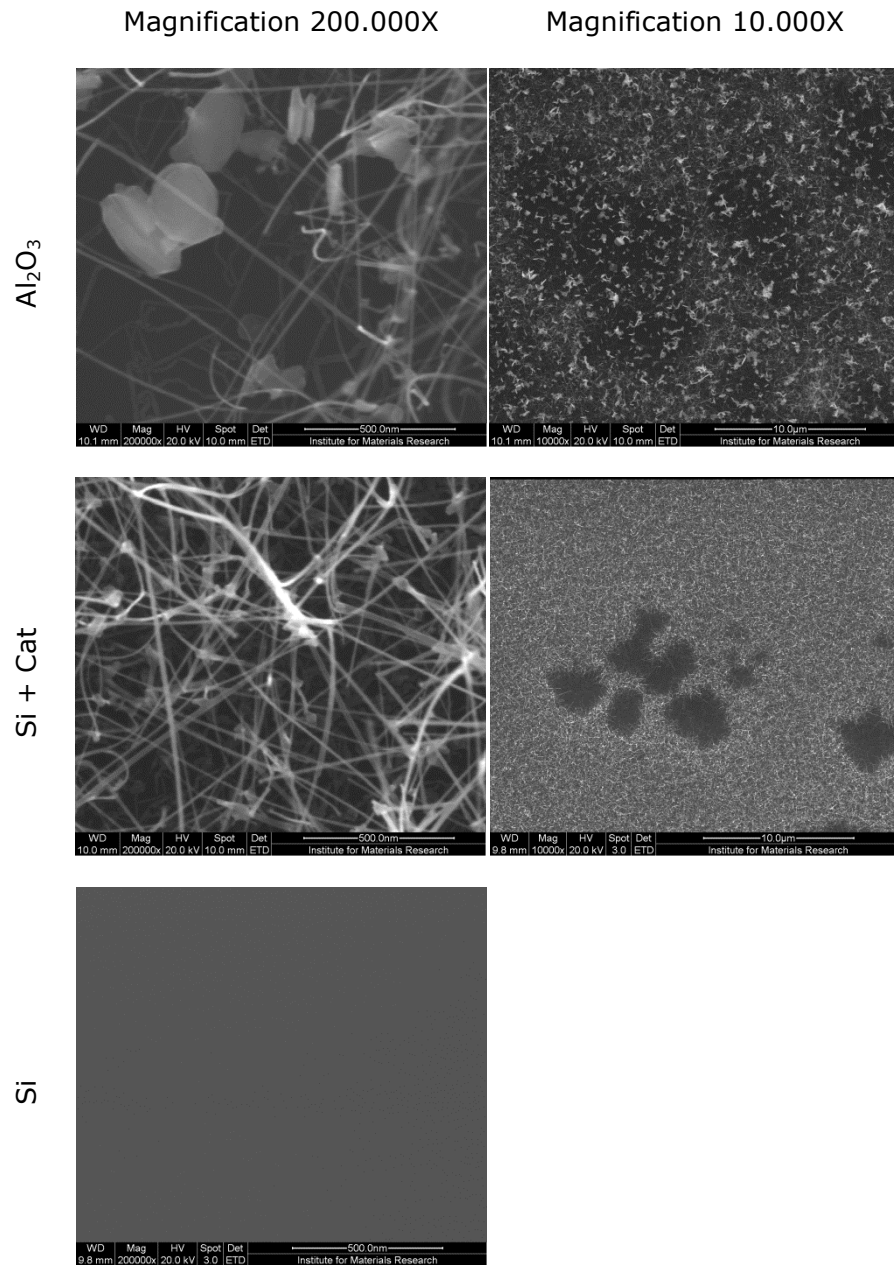

Figure 21 illustrates the difference in formation of nanowires using an Al2O3 substrate with catalyst vs. silicon surface with and without catalyst (all position P4) for two different magnifications

Growth mode

After determining what conditions are needed to synthesize the nanowires and knowing that the catalyst is crucial for the growth, the type of growth has to be determined. Figure 22 shows that the catalyst particle residing on top of the wire has a faceted shape. This is indicative for a Vapor-Solid-Solid (VSS) growth mode which occurs at reduced temperatures where the formation of a supersaturated solution takes place in the solid state of the

catalyst particle. As a consequence, smaller diameters of the growing nanowires can be expected as the catalyst particle does not swell upon dissolution of the precursor material as much as in case of a liquid catalyst particle which works at much higher temperatures where the solubility is increased (VLS growth mode). Thus, nanowire diameters below 10nm appear realistic thereby allowing to enter the size regime where quantum effects like electron or phonon confinement start to influence all physical and chemical properties of the wires.

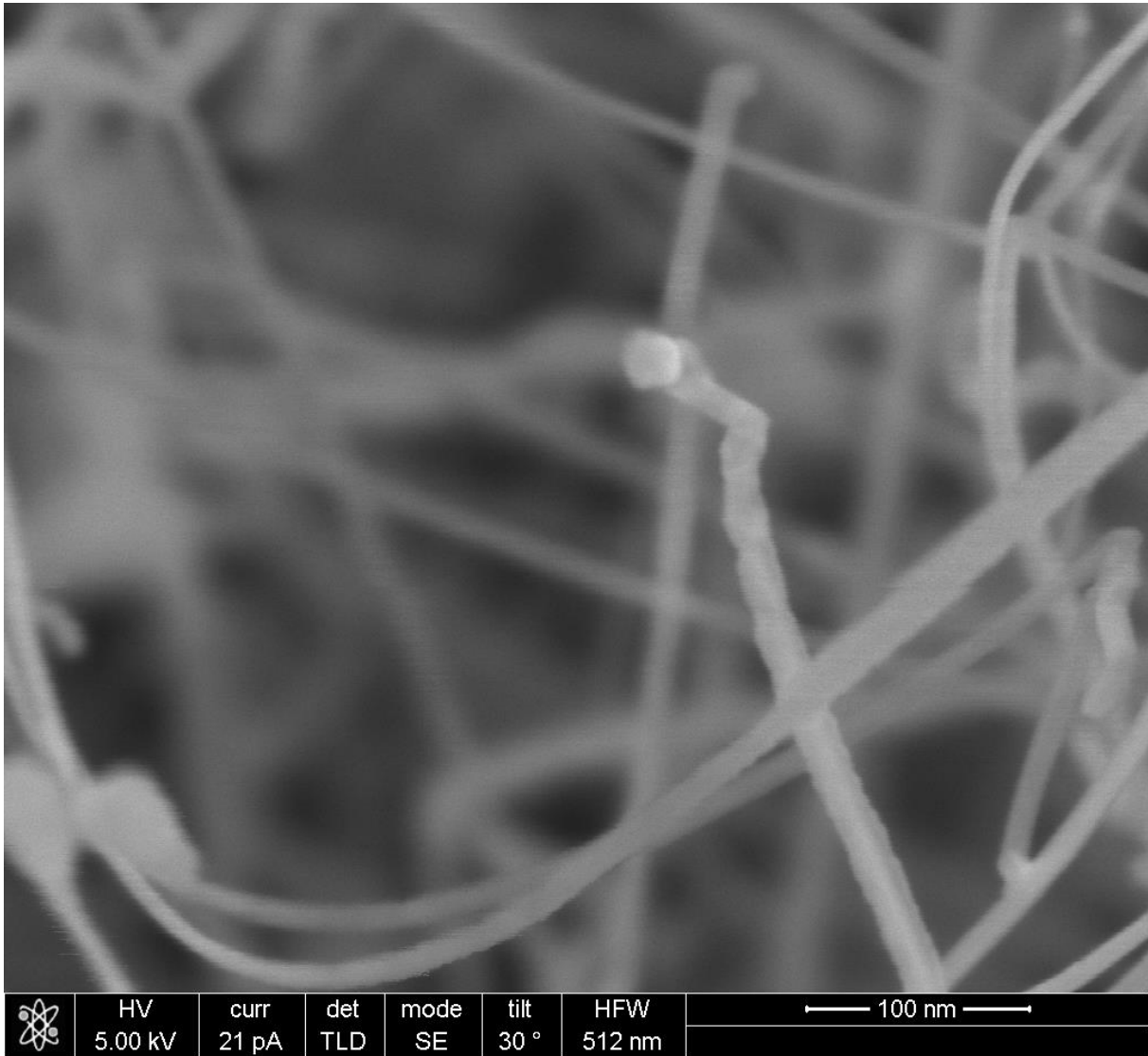|	HV	curr	det	mode	tilt	HFW	——— 100 nm ———
	5.00 kV	21 pA	TLD	SE	30 °	512 nm	

Figure 22: high resolution SEM image (measured in the group of Prof. C. Ronning, Jena University) indicating a VSS (Vapour-Solid-Solid) growth mechanism due to the appearance of facets at the catalyst particle surface. In case of VLS (Vapour-Liquid-Solid) growth mode a spherical droplet forming the catalyst is expected instead.

Size control

The final step to be performed after fine tuning the conditions for an efficient growth has to be the investigation of the dependency of the resulting nanowire diameter on the catalyst size. One sample resulting from every micellar solution was placed on the ceramic disk and positioned at P4 to grow wires. SEM images at a magnification of 200.000X were subsequently analysed by imageJ to extract the wire diameter. Figure 23 show an image revealing several nanowires which are individually labelled and characterized to allow the calculating of the average diameter.
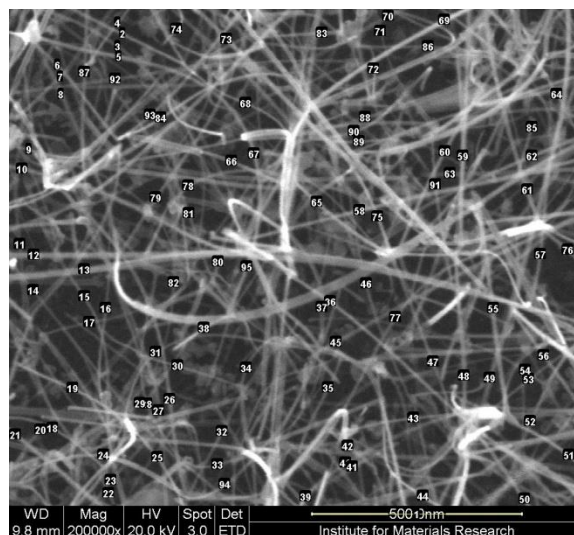

Figure 23 illustrates how the average diameter of a sample was determined. Images containing less than a minimum of 10 wires were discarded and the appropriate sample was remeasured.

The diameter of each of these wires is than averaged per sample and the result of the average diameter versus the diameter of the catalyst particles is plotted in Figure 24. The graph indicates a rather linear dependency of the catalyst particle size versus the diameter of the wires. However, more experiments are required based on particle diameters below 2.5 nm to better establish the functional relationship between the two properties over the whole size range. Despite the large scatter in the experimental results, Figure 24 clearly demonstrates that the diameter of SnO_2 nanowires can actually be controlled using size-selected micellar catalyst particles. ***That way, nanowires with controllable diameters well below 10 nm appear realistic which could allow to enter the size (diameter) regime where quantum confinement effects of electrons and phonons become increasingly important.***
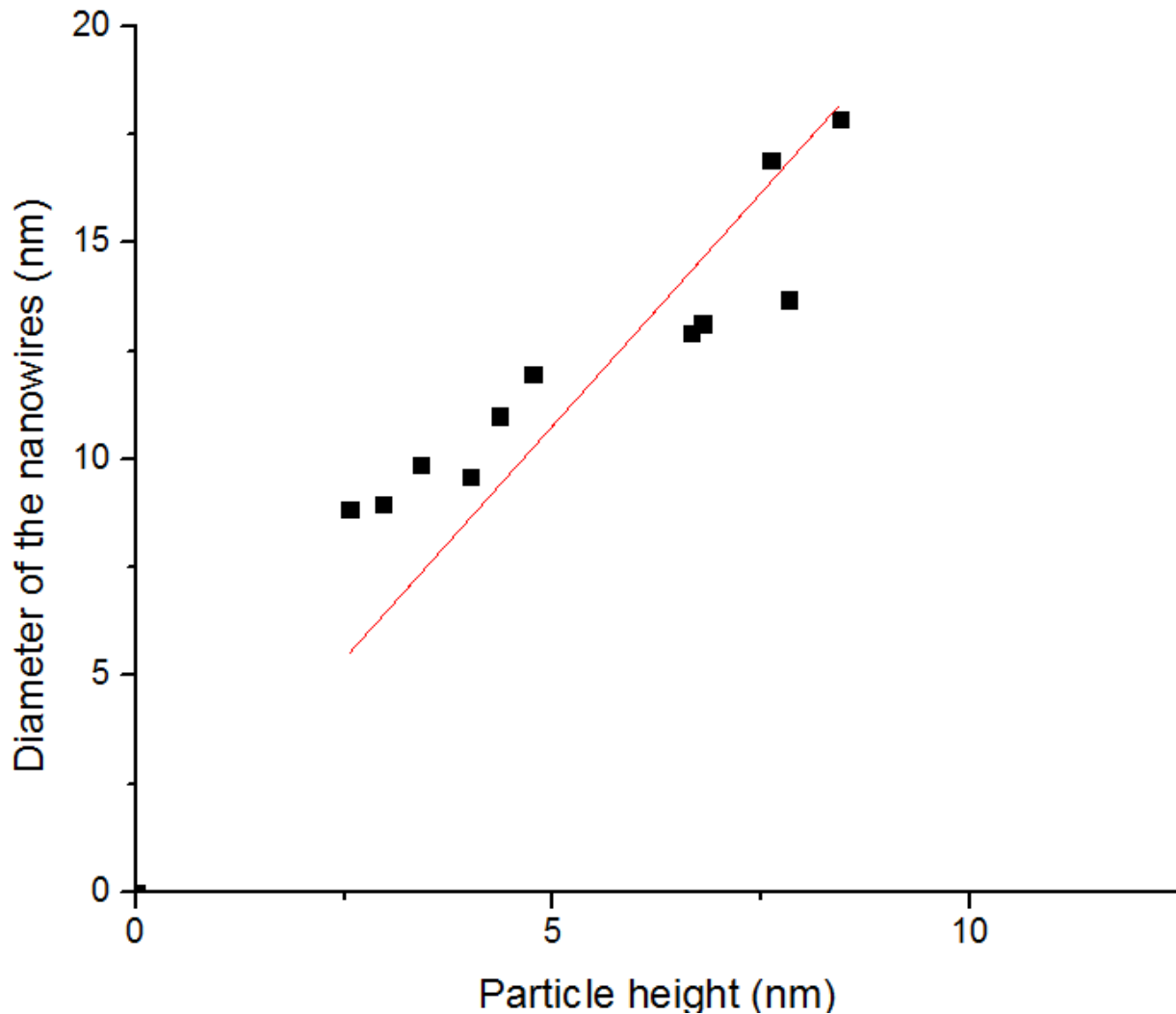
Figure 24 shows that the diameter of the nanowires depend linearly on the diameter of the catalyst particle used for growth. With the diameter of the wirers increasing 2,15 times as fast as the diameter of the average particle height.

Characterization of the nanowires

EDX

The SEM apparatus has the ability to measure EDX spectra thus allowing a chemical analysis of the grown nanostructures. For the SnO_2 nanowire sample tested here, a clear Sn Peak can be recognized at an energy of 3,6 keV (Figure 25). In this scan some additional (minor) peaks appear which indicate other elements to be present at the sample surface. These elements only show up in traces and supposedly do not influence the growth mechanism or the wires themselves. The carbon peak appearing around 0,35 keV is most likely due to residue left from the carbothermal reduction reaction.
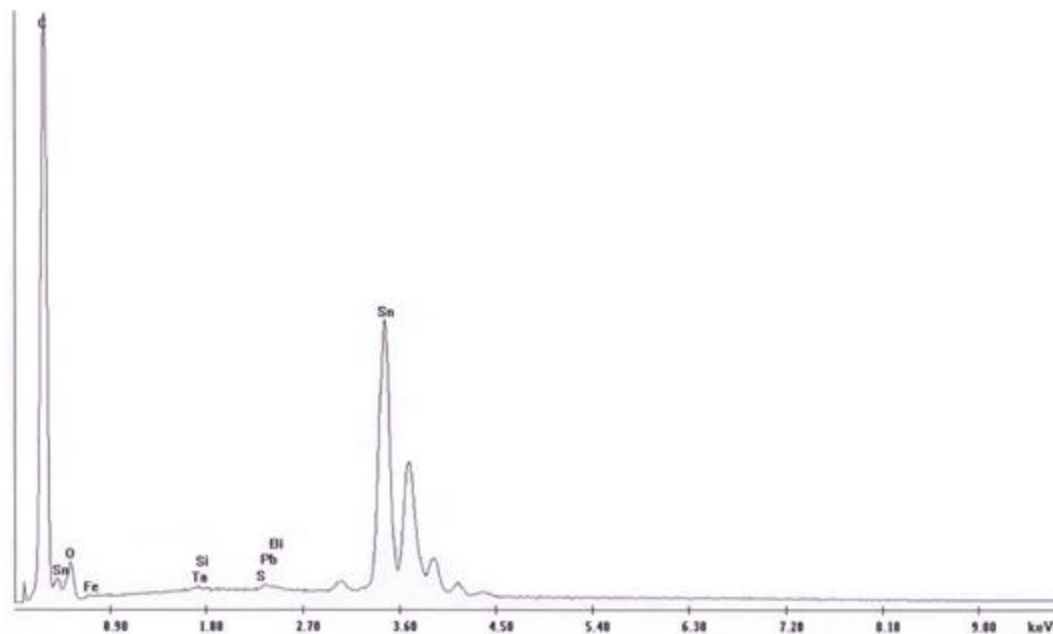
Figure 25: EDX scan from one of the nanowire samples acquired over an extended time period to improve the sensitivity of the chemical analysis.

Raman

Figure 26 presents first results from Raman spectroscopy experiments performed on samples with different diameters (9,8 nm, 17 nm) of the SnO_2 nanowires. The peak at 521 cm^{-1} arises from the substrate (Si), whereas the Raman lines at 475, 634 and 775 cm^{-1} correspond to the E_g, A_{1g} and B_{2g} Raman modes of SnO_2, respectively.[66] In the spectrum acquired on the nanowires with larger average diameter, on one hand, an additional peak around 691 cm^{-1} is detected which is not present in the spectrum on the thinner nanowires possibly due to a decrease in IR activity because of the small size.[67] On the other hand, the spectrum arising from the thinner wires also reveals the existence of additional peaks at positions of about 303 cm^{-1} and 813 cm^{-1} whose origin is not clear yet. During the Raman scans also signs of photoluminescence toward the red side of the spectrum where seen, [67] but due to time restrictions not recorded.
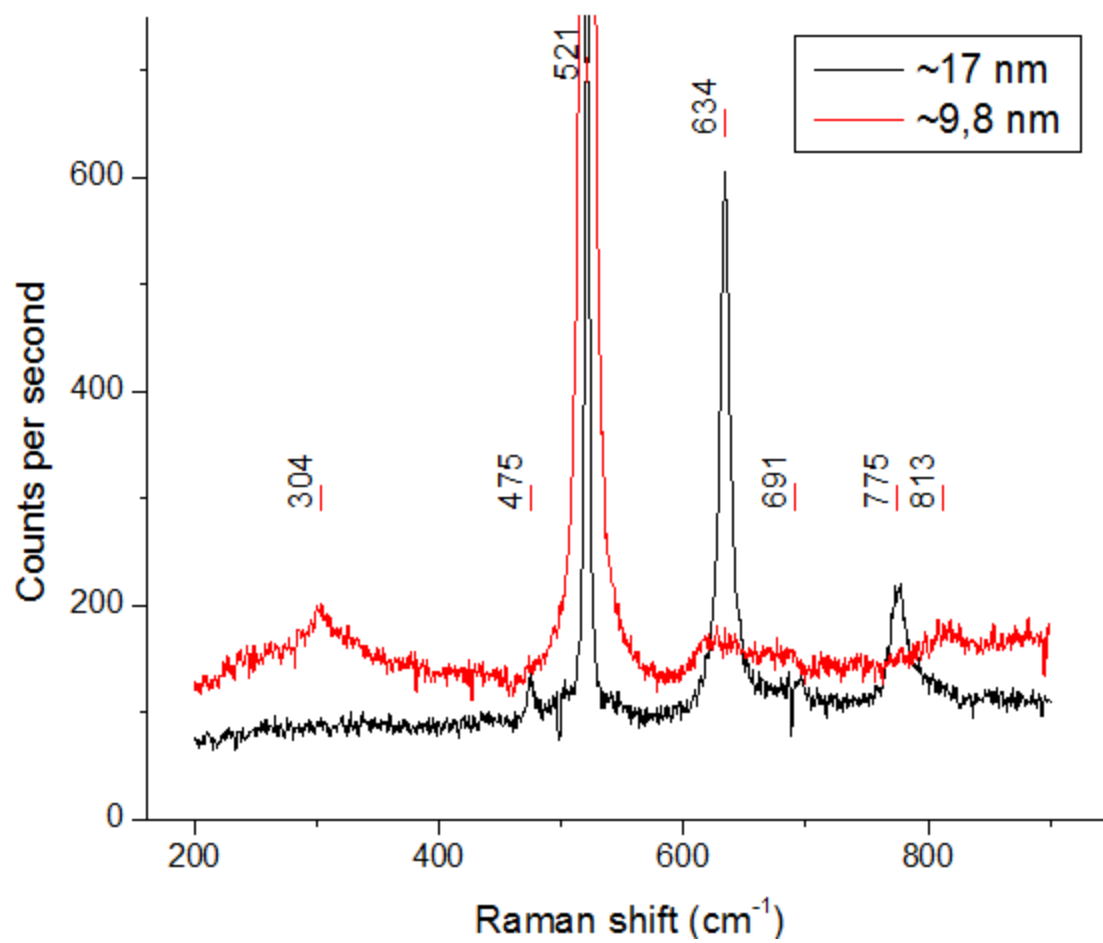
Figure 26 represents the Raman spectrum taken for nanowire samples with different diameters. All spectra are recorded with a magnification of 100X, the acquisition time for the thicker wires was 3x60 s, for the small diameter wires 2x120 s.

Conclusion

The formation of SnO$_2$ nanowires by chemical vapour deposition is a process that itself depends on many parameters. Some of these parameters are easily accessible but sometimes overlooked like the furnace (used for heating and evaporating the precursor material) with its own temperature profile. A second temperature that will be of great importance is the condensation temperature of the substrate which carries the catalyst particles. Of high importance are also the details of the arrangement of the glassware forming a mayor part of the furnace: the arrangement of the quartz tube or tubes that are used to create the single or double tube systems all having their own sizes and thicknesses. Here, small changes in these sizes can already lead to a change in the flow pattern inside the tube(s). Jet another property is the type of precursor; Sn, SnO, SnO$_2$ or SnO$_2$ + C all having the similar effects but under different experimental conditions. Not to forget about the actual gas applied at a certain flow, with or without a vacuum system in parallel. All these parameters have to be considered and tested before the first nanowires are grown in the availabe setup. For this reason the found most important parameters reported here will differ from those reported in literature (Table 1). For this work the optimum conditions are evaporation of the source material at a temperature of 1000 °C, and a substrate temperature between 628 and 482 °C for an optimized deposition. The flow rate is best kept constant at 100 sccm while growing for about 2 H. The nanowires start to form in the first minute after reaching the evaporation temperature but to make use of the wires themselves longer wires are needed implying significantly longer growth times.

After localizing and optimizing all relevant parameters SnO$_2$ nanowires could finally be grown combining the flexibility of the micellar technique to deposit highly controllable catalyst particle arrays with the VSS method working at lower temperature than the commonly used VLS technique. This allows to control the diameter of the nanowires by adjusting the size of the gold catalyst particles. A small sized catalyst particle will produce nanowires with a small diameter while bigger particles will produce bigger diameters. This approach allowed us the controlled growth of nanowires with diameters approaching and even passing beyond the critical value of 10 nm, where quantum size effects like electron confinement starts to play an increasingly important role thereby influencing all physical and chemical properties of the wires many of them still being unexplored. What could not be achieved in this work is the controlled alignment of all the wires in one direction by growing them on either a silicon substrate or on a aluminium thin film in contrast to reports by other groups which, however, frequently exploit the VLS growth mode.

Nanowires with still smaller diameters then realized here can be expected using different copolymers or an improved loading of the micellar nanoreactors with metal salt. For future applications a highly ordered array might be created by growing on a TiO$_2$ substrate that will allow the formation of ultra-high density forests of nanowires with highly controllable diameter which should allow the tailoring of specific physical and/or chemical properties of such wires targeting specific applications like bio- or chemosensing where high surface-to-volume ratios are required.

References

1. Feynman R. There's plenty of room at the bottom. Engineering and science. 1960;23(5):22-36.
2. (cgpm) Gdpem. Comptes Rendus de la 11^e Resolution 121961. p. 87.
3. Xia Y, Yang P, Sun Y, Wu Y, Mayers B, Gates B, et al. One-Dimensional Nanostructures: Synthesis, Characterization, and Applications. Advanced Materials. 2003;15(5):353-89.
4. Hayden O, Agarwal R, Lieber CM. Nanoscale avalanche photodiodes for highly sensitive and spatially resolved photon detection. Nat Mater. 2006;5(5):352-6.
5. Zhibo Zhang JYYaMSD. Bismuth quantum-wire arrays fabricated by a vacuum melting and pressure injection process. Journal of Materials Research. 1998;13:1745-8
6. Hochbaum AI, Yang P. Semiconductor Nanowires for Energy Conversion. Chemical Reviews. 2009;110(1):527-46.
7. Toimil-Molares ME. Characterization and properties of micro- and nanowires of controlled size, composition, and geometry fabricated by electrodeposition and ion-track technology. Beilstein Journal of Nanotechnology. 2012;3:860-83.
8. Patolsky F, Timko BP, Zheng G, Lieber CM. Nanowire-Based Nanoelectronic Devices in the Life Sciences. MRS Bulletin. 2007;32(02):142-9.
9. Barth S, Hernandez-Ramirez F, Holmes JD, Romano-Rodriguez A. Synthesis and applications of one-dimensional semiconductors. Progress in Materials Science. 2010;55(6):563-627.
10. Wang X, Li Y. Rare-Earth-Compound Nanowires, Nanotubes, and Fullerene-Like Nanoparticles: Synthesis, Characterization, and Properties. Chemistry – A European Journal. 2003;9(22):5627-35.
11. Goetzberger A, Hebling C. Photovoltaic materials, past, present, future. Solar Energy Materials and Solar Cells. 2000;62(1–2):1-19.
12. R.L. Mishra SKM, S. G. Prakash. Optical and gas sensing characteristics of tin oxide nano-crystalline thin film. journal of Ovonic Research. 2009;5(4):77 - 85.
13. Gad-el-Hak M. The MEMS handbook. Boca Raton, FL: CRC Press; 2002.
14. Chen R, Xing GZ, Gao J, Zhang Z, Wu T, Sun HD. Characteristics of ultraviolet photoluminescence from high quality tin oxide nanowires. Applied Physics Letters. 2009;95(6):061908.
15. Cheng C, Liu B, Yang H, Zhou W, Sun L, Chen R, et al. Hierarchical Assembly of ZnO Nanostructures on SnO2 Backbone Nanowires: Low-Temperature

Hydrothermal Preparation and Optical Properties. ACS Nano. 2009;3(10):3069-76.

16. Zhang Z, Gao J, Wong LM, Tao JG, Liao L, Zheng Z, et al. Morphology-controlled synthesis and a comparative study of the physical properties of SnO 2 nanostructures: from ultrathin nanowires to ultrawide nanobelts. Nanotechnology. 2009;20(13):135605.

17. Tennakone K, R. R. A. Kumara G, R. M. Kottegoda I, P. S. Perera V. An efficient dye-sensitized photoelectrochemical solar cell made from oxides of tin and zinc. Chemical Communications. 1999;0(1):15-6.

18. Liu J, Li Y, Huang X, Ding R, Hu Y, Jiang J, et al. Direct growth of SnO2 nanorod array electrodes for lithium-ion batteries. Journal of Materials Chemistry. 2009;19(13):1859-64.

19. Du N, Zhang H, Yu J, Wu P, Zhai C, Xu Y, et al. General Layer-By-Layer Approach To Composite Nanotubes and Their Enhanced Lithium-Storage and Gas-Sensing Properties. Chemistry of Materials. 2009;21(21):5264-71.

20. Feng J-J, Zhu J-T, Xu J-J, Chen H-Y. Enhanced Biosensing Performance of Mesoporous SnO2 Multilayer Film in Interfacing Hemoglobin. Journal of Nanoscience and Nanotechnology. 2009;9(4):2290-6.

21. Ansari AA, Kaushik A, Solanki PR, Malhotra BD. Electrochemical Cholesterol Sensor Based on Tin Oxide-Chitosan Nanobiocomposite Film. Electroanalysis. 2009;21(8):965-72.

22. Jia NQ, Xu J, Sun MH, Jiang ZY. A Mediatorless Hydrogen Peroxide Biosensor Based on Horseradish Peroxidase Immobilized in Tin Oxide Sol-Gel Film. Analytical Letters. 2005;38(8):1237-48.

23. Liu J, Li Y, Huang X, Zhu Z. Tin Oxide Nanorod Array-Based Electrochemical Hydrogen Peroxide Biosensor. Nanoscale Research Letters. 2010;5(7):1177-81.

24. Yan R, Park J-H, Choi Y, Heo C-J, Yang S-M, Lee LP, et al. Nanowire-based single-cell endoscopy. Nat Nano. 2012;7(3):191-6.

25. Hieu NV, Loan LTN, Khoang ND, Minh NT, Viet DT, Minh DC, et al. A facile thermal evaporation route for large-area synthesis of tin oxide nanowires: Characterizations and their use for liquid petroleum gas sensor. Current Applied Physics. 2010;10(2):636-41.

26. Kolmakov A, Moskovits M. CHEMICAL SENSING AND CATALYSIS BY ONE-DIMENSIONAL METAL-OXIDE NANOSTRUCTURES. Annual Review of Materials Research. 2004;34(1):151-80.

27. Po-Chiang C, Guozhen S, Chongwu Z. Chemical Sensors and Electronic Noses Based on 1-D Metal Oxide Nanostructures. Nanotechnology, IEEE Transactions on. 2008;7(6):668-82.

28. Mathur S, Barth S, Shen H, Pyun J-C, Werner U. Size-Dependent Photoconductance in SnO2 Nanowires. Small. 2005;1(7):713-7.
29. Hernández-Ramírez F, Tarancón A, Casals O, Rodríguez J, Romano-Rodríguez A, Morante JR, et al. Fabrication and electrical characterization of circuits based on individual tin oxide nanowires. Nanotechnology. 2006;17(22):5577.
30. Kataura H, Kumazawa Y, Maniwa Y, Umezu I, Suzuki S, Ohtsuka Y, et al. Optical properties of single-wall carbon nanotubes. Synthetic Metals. 1999;103(1–3):2555-8.
31. Gall K, Diao J, Dunn ML. The Strength of Gold Nanowires. Nano Letters. 2004;4(12):2431-6.
32. McEuen PLF, M.S. Hongkun Park. Single-Walled Carbon Nanotube Electronics. The IEEE Transactions on Nanotechnology. 2002;1(1):78-85.
33. McDowell MT, Leach AM, Gall K. On The Elastic Modulus of Metallic Nanowires. Nano Letters. 2008;8(11):3613-8.
34. Whitney TM, Searson PC, Jiang JS, Chien CL. Fabrication and Magnetic Properties of Arrays of Metallic Nanowires. Science. 1993;261(5126):1316-9.
35. Lu HM, Han FQ, Meng XK. Size-Dependent Thermodynamic Properties of Metallic Nanowires. The Journal of Physical Chemistry B. 2008;112(31):9444-8.
36. Cornelius TW, Toimil-Molares ME. Finite- and Quantum-Size Effects of Bismuth Nanowires2010 2010-02-01.
37. Farhangfar S. Quantum size effects in a one-dimensional semimetal. Physical Review B. 2006;74(20):205318.
38. Balzani V, Credi A, Venturi M. The Bottom-Up Approach to Molecular-Level Devices and Machines. Chemistry – A European Journal. 2002;8(24):5524-32.
39. Hyunjin L, Lee-eun Y, Seong-Wan R, Jin-Woo H, Kanghoon J, Dong-Yoon J, et al., editors. Sub-5nm All-Around Gate FinFET for Ultimate Scaling. VLSI Technology, 2006 Digest of Technical Papers 2006 Symposium on; 2006 0-0 0.
40. Fuechsle M, MahapatraS, Zwanenburg FA, Friesen M, Eriksson MA, Simmons MY. Spectroscopy of few-electron single-crystal silicon quantum dots. Nat Nano. 2010;5(7):502-5.
41. Intel. Intel® 22nm Technology. intel; 2011 [cited 2013 6-7].
42. Cormack PAG, Elorza AZ. Molecularly imprinted polymers: synthesis and characterisation. Journal of Chromatography B. 2004;804(1):173-82.

43. O'Reilly RK, Hawker CJ, Wooley KL. Cross-linked block copolymer micelles: functional nanostructures of great potential and versatility. Chemical Society Reviews. 2006;35(11).

44. Kästle G, Boyen HG, Weigl F, Lengl G, Herzog T, Ziemann P, et al. Micellar Nanoreactors—Preparation and Characterization of Hexagonally Ordered Arrays of Metallic Nanodots. Advanced Functional Materials. 2003;13(11):853-61.

45. Carrot G, Valmalette JC, Plummer CJG, Scholz SM, Dutta J, Hofmann H, et al. Gold nanoparticle synthesis in graft copolymer micelles. Colloid and Polymer Science. 1998;276:853-9.

46. Chan YNC, Schrock RR, Cohen RE. Synthesis of silver and gold nanoclusters within microphase-separated diblock copolymers. Chemistry of Materials. 1992;4(1):24-7.

47. Lu J, Yi SS, Kopley T, Qian C, Liu J, Gulari E. Fabrication of Ordered Catalytically Active Nanoparticles Derived from Block Copolymer Micelle Templates for Controllable Synthesis of Single-Walled Carbon Nanotubes. The Journal of Physical Chemistry B. 2006;110(13):6655-60.

48. Yue J, Sankaran V, Cohen RE, Schrock RR. Interconversion of ZnF_2 and ZnS nanoclusters within spherical microdomains in block copolymer films. Journal of the American Chemical Society. 1993;115(10):4409-10.

49. Wagner RS, Ellis WC. VAPOR-LIQUID-SOLID MECHANISM OF SINGLE CRYSTAL GROWTH. Appl Phys Lett. 1964;4(5):89-90.

50. Kim W-S, Kim D, Choi KJ, Park J-G, Hong S-H. Epitaxial Directional Growth of Tin Oxide (101) Nanowires on Titania (101) Substrate. Crystal Growth & Design. 2010;10(11):4746-51.

51. Wang JX, Liu DF, Yan XQ, Yuan HJ, Ci LJ, Zhou ZP, et al. Growth of SnO_2 nanowires with uniform branched structures. Solid State Communications. 2004;130(1–2):89-94.

52. Mazeina L, Picard YN, Caldwell JD, Glaser ER, Prokes SM. Growth and photoluminescence properties of vertically aligned SnO_2 nanowires. Journal of Crystal Growth. 2009;311(11):3158-62.

53. Ma Y-J, Zhou F, Lu L, Zhang Z. Low-temperature transport properties of individual SnO_2 nanowires. Solid State Communications. 2004;130(5):313-6.

54. Sberveglieri G, Concina I, Comini E, Falasconi M, Ferroni M, Sberveglieri V. Synthesis and integration of tin oxide nanowires into an electronic nose. Vacuum. 2012;86(5):532-5.

55. Trung DD, Van Toan N, Van Tong P, Van Duy N, Hoa ND, Hieu NV. Synthesis of single-crystal SnO2 nanowires for NOx gas sensors application. Ceramics International. 2012;38(8):6557-63.
56. Kim W-S, Kim D-H, Jang Y-G, Hong S-H. Synthesis of well-aligned SnO2 nanowires with branches on r-cut sapphire substrate. CrystEngComm. 2012;14(5):1545-9.
57. Johnson MC, Aloni S, McCready DE, Bourret-Courchesne ED. Controlled VLS Growth of Indium, Gallium and Tin Oxide Nanowires via Chemical Vapor Transport. 2006.
58. Gao J, Lebedev OI, Turner S, Li YF, Lu YH, Feng YP, et al. Phase Selection Enabled Formation of Abrupt Axial Heterojunctions in Branched Oxide Nanowires. Nano Letters. 2011;12(1):275-80.
59. Kar A, Stroscio MA, Dutta M, Kumari J, Meyyappan M. Growth and properties of tin oxide nanowires and the effect of annealing conditions. Semiconductor Science and Technology. 2010;25(2):024012.
60. Spatz JP, Sheiko S, Möller M. Ion-Stabilized Block Copolymer Micelles: Film Formation and Intermicellar Interaction. Macromolecules. 1996;29(9):3220-6.
61. Spatz JP, Mössmer S, Hartmann C, Möller M, Herzog T, Krieger M, et al. Ordered Deposition of Inorganic Clusters from Micellar Block Copolymer Films. Langmuir. 1999;16(2):407-15.
62. Nečas D, Klapetek P. Gwyddion: an open-source software for SPM data analysis. centreurjphys. 2012;10(1):181-8.
63. Crist BV. The Elements and Native Oxides. Handbooks of Monochramatic XPS Spectra: XPS international, inc; 1999.
64. Geng C, Jiang Y, Yao Y, Meng X, Zapien JA, Lee CS, et al. Well-Aligned ZnO Nanowire Arrays Fabricated on Silicon Substrates. Advanced Functional Materials. 2004;14(6):589-94.
65. Rasband WS. ImageJ. 1.46r ed. Bethesda, Maryland, USA: U.S. National Institutes of Health; 1997-2012.
66. Peercy PS, Morosin B. Pressure and Temperature Dependences of the Raman-Active Phonons in SnO_{2}. Physical Review B. 1973;7(6):2779-86.
67. Zhou JX, Zhang MS, Hong JM, Yin Z. Raman spectroscopic and photoluminescence study of single-crystalline SnO2 nanowires. Solid State Communications. 2006;138(5):242-6.

Supplement

Supplement 1

- Ultra sound Protocol
- Clean the glass flask and the knife with toluene and dry them in a nitrogen jet.
- Add 25 mg of the short polymer in the nitrogen glove box in the flask.
- Calculate the desired amount of gold salt ($HAuCl_4$ xH_2O) to add to the flask based on the actual amount of polymer added and the desired loading ratio.
- Add the calculated amount of salt to the polymer in the flask.
- Close the flask and bring it back to ambient air.
- Add 5 ml of extra dry toluene to the flask and close it again.
- Place the flask inside the US bath and turn it to maximum (position 9).
- Switch on the US bath for 2 H
- Every 30 minutes check for changes in temperature of the water of the bath and if needed bring it back down to room temperature by exchanging some of the warm demi water for cold.
- After 2H in the US bath one can take out the flask and dry the outside.
- Dip coat your samples ASAP.

Supplement 2

Origin import script for particle size distribution

```
aaa$= page.longname$;
aaa.Replace(".txt", );
b$=\;
c$=distri;
d$=aaa$+b$+c$;
col(B)=col(A)*1E9;
colstats irng:=col(B);
wks.name$ = Results;
page.active = 1;
wks.colSel(2,1);
run.section(plot,histogram);
get %C -hbb lower;
get %C -hbe upper;
set %C -hbs $((upper-lower)/25);
pe_mkdir(d$);
pe_move move:= %H path:= d$;
page.active = 2;
pe_move move:= %H path:= d$;
```

Import for inter-particle distance

```
aaa$= page.longname$;
aaa.Replace(" i.txt", );
b$=\;
c$=inter;
d$=aaa$+b$+c$;
```

```
col(A)=col(A)*1E9;
col(C)=col(C)*1E9;
col(E)=col(E)*1E9;
col(B)=col(B)*1E21;
col(D)=col(D)*1E21;
col(F)=col(F)*1E21;
range rin=(1,2);range routx = 7;pkfind iy:=rin dir:=p
method:=max npts:=2 filter:=h
value:=0.1ocenter:=<none> ocenter_x:=routx;
range rin=(3,4);range routx = 8;pkfind iy:=rin dir:=p
method:=max npts:=2 filter:=h
value:=0.1ocenter:=<none> ocenter_x:=routx ;
range rin=(5,6);range routx = 9;pkfind iy:=rin dir:=p
method:=max npts:=2 filter:=h
value:=0.1ocenter:=<none> ocenter_x:=routx;
col(J)=diff(col(G));
col(K)=diff(col(H));
col(L)=diff(col(I));
wstackcol irng:=col(J:L);
colstats irng:= col(B);
wks.name$ = results;
page.active = 1;
plotxy iy:=((1,2), (3,4),(5,6)) plot:=200;
pe_mkdir(d$);
pe_move move:= %H path:= d$;
page.active = 3;
pe_move move:= %H path:= d$;
```

Supplement 3: Density problems

On the SEM images taken at a low magnification a difference could be seen in the growth density of the wires, as has already been indicated in the section about micelles above. In this section two explanations were given, a wetting problem during dip coating or an alternative explanation is that the seeding density of the catalyst particles is uniform, but that the tin vapor is not arriving in an uniform way on the sample. Some of the SEM images do show a density deformations that seem be regular in high and low densities resembling a standing wave patron as can be seen in Figure 27A. To determine the role of the flow, its direction was marked an SEM images where taken with so that the flow would come in at the top of the image. Figure 27B shows one of these images, again the wave patron can be recognized however the patron is in the wrong direction. This direction however is the same as is used for dipcoating the sample confirming that there is a wetting problem of some samples.
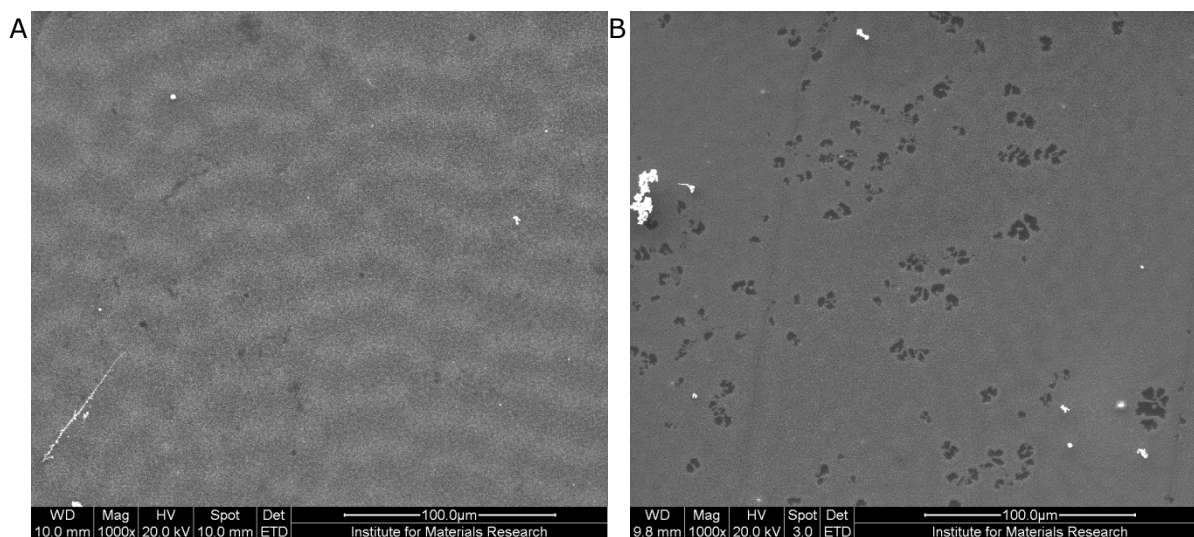

Figure 27 represents the density problem that becomes visible on some of the lower SEM magnification the areas with higher density and lower density seem to be showing a wave patron (A). Image B shows an SEM image taken from a sample in which the gas flow if from the top of the image to the bottom. The wave patron visual on the image is horizontal.

Supplement 4: Self-catalyzed growth of fibers

During some of the growth experiments a gray fiber structure appeared hanging downwards inside the semi closed inliner (Figure 28A). In addition to these gray fibers in a few cases some additional white fiber structures appeared to grow starting from the ceramic disk. In some occasions the length of these fiber structures were up to 3 cm. To get a more detailed insight into these fibers, they were analyzed by SEM as can be seen in Figure 28C and D. Figure 28B shows the EDX scan to determine the composition of the fibers. These images show that the fibers are made out of nanowires as well, but comparing these wires to the wires made from gold catalyst particles the latter allow to control their diameter by means of the catalyst size.
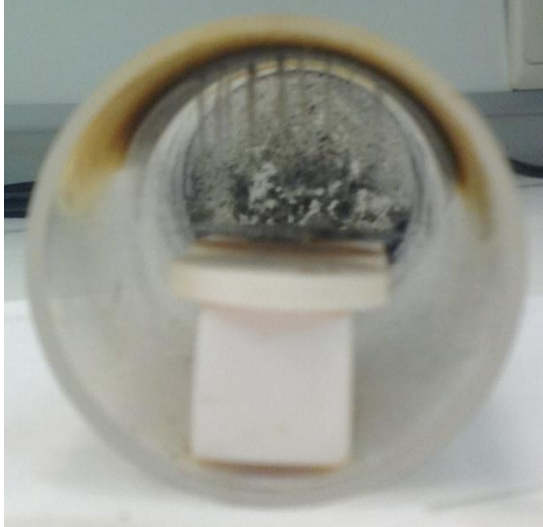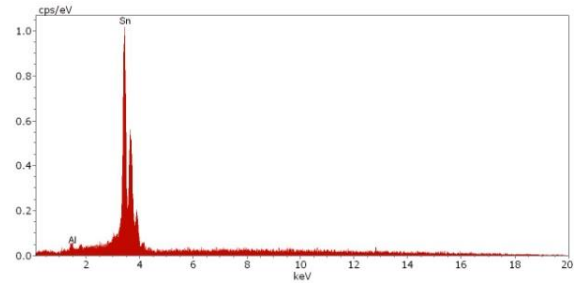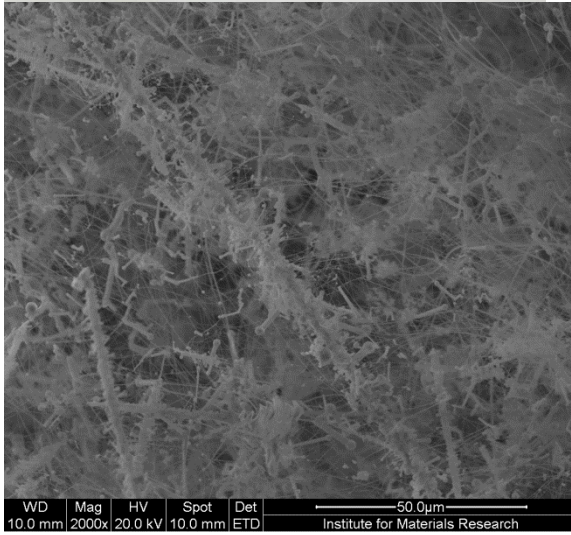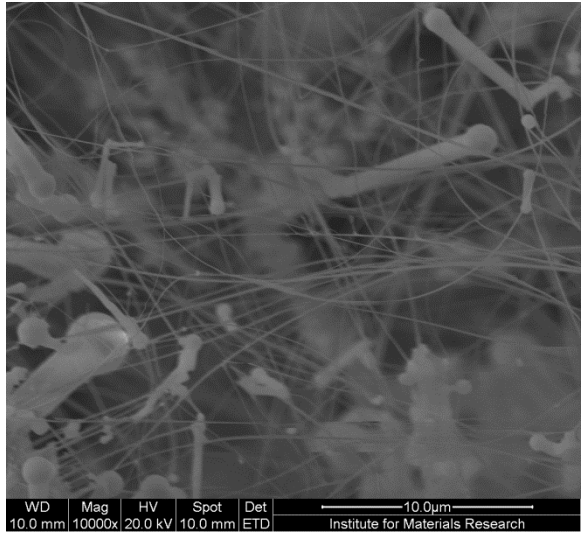
Figure 28A shows the fiber structure hanging down from the top of the inliner. B is the EDX spectra taken from the fibers, C and D are SEM images of the fibers at a magnification of 2.000X and 10.000X respectively.

Auteursrechtelijke overeenkomst

Ik/wij verlenen het wereldwijde auteursrecht voor de ingediende eindverhandeling:
Synthesis and characterization of arrays of metal oxide nanowires with highly controllable diameters for future sensor applications

Richting: **master in de biomedische wetenschappen-bio-elektronica en nanotechnologie**
Jaar: **2013**

in alle mogelijke mediaformaten, - bestaande en in de toekomst te ontwikkelen - , aan de Universiteit Hasselt.

Niet tegenstaand deze toekenning van het auteursrecht aan de Universiteit Hasselt
behoud ik als auteur het recht om de eindverhandeling, - in zijn geheel of gedeeltelijk -,
vrij te reproduceren, (her)publiceren of distribueren zonder de toelating te moeten
verkrijgen van de Universiteit Hasselt.

Ik bevestig dat de eindverhandeling mijn origineel werk is, en dat ik het recht heb om de rechten te verlenen die in deze overeenkomst worden beschreven. Ik verklaar tevens dat de eindverhandeling, naar mijn weten, het auteursrecht van anderen niet overtreedt.

Ik verklaar tevens dat ik voor het materiaal in de eindverhandeling dat beschermd wordt door het auteursrecht, de nodige toelatingen heb verkregen zodat ik deze ook aan de Universiteit Hasselt kan overdragen en dat dit duidelijk in de tekst en inhoud van de eindverhandeling werd genotificeerd.

Universiteit Hasselt zal mij als auteur(s) van de eindverhandeling identificeren en zal geen wijzigingen aanbrengen aan de eindverhandeling, uitgezonderd deze toegelaten door deze overeenkomst.

Voor akkoord,

Betlem, Kaï

Datum: **13/06/2013**